

1 **KDM6 demethylases contribute to EWSR1-FLI1-driven oncogenic**  
2 **transformation in Ewing Sarcoma**

3 Elisabet Figuerola-Bou<sup>1‡</sup>, Carla Rios-Astorch<sup>1‡</sup>, Enrique Blanco<sup>2,3</sup>, María Sánchez-  
4 Jiménez<sup>1</sup>, Pablo Táboas<sup>1</sup>, Guerau Fernández<sup>4</sup>, Soledad Gómez<sup>1</sup>, Oscar Muñoz<sup>1</sup>, Pol  
5 Castellano-Escuder<sup>5</sup>, Sara Pérez-Jaume<sup>1, 6</sup>, Marta García<sup>1</sup>, Estela Prada<sup>1</sup>, Silvia Mateo-  
6 Lozano<sup>1</sup>, Nicolo Riggi<sup>7,8</sup>, Alexandra Avgustinova<sup>1,9</sup>, Cinzia Lavarino<sup>1,10</sup>, Luciano Di  
7 Croce<sup>2,3,11</sup>, Sara Sánchez-Molina<sup>1\*†</sup> and Jaume Mora<sup>1,10\*†</sup>

---

<sup>1</sup>Pediatric Cancer, Institut de Recerca Sant Joan de Déu (IRSJD); Esplugues de Llobregat (Barcelona), 08950, Spain.

<sup>2</sup>Center for Genomic Regulation (CRG), Barcelona Institute of Science and Technology; Barcelona, 08003, Spain.

<sup>3</sup>Universitat Pompeu Fabra (UPF); Barcelona, 08002, Spain.

<sup>4</sup>Molecular Genetics Department, Institut de Recerca Sant Joan de Déu; Esplugues de Llobregat (Barcelona), 08950, Spain.

<sup>5</sup>Biomarkers and Nutritional & Food Metabolomics Research Group, Department of Nutrition, Food Science and Gastronomy, University of Barcelona; Barcelona, 08028, Spain.

<sup>6</sup>Biostatistics Unit, Department of Clinical Practice, University of Barcelona; Barcelona, 08036, Spain.

<sup>7</sup>Institute of Pathology, Centre Hospitalier Universitaire Vaudois, Faculty of Biology and Medicine, University of Lausanne; Lausanne, 1004, Switzerland.

<sup>8</sup>Department of Cell and Tissue Genomics, Genentech Inc; South San Francisco, California, 94080, USA.

<sup>9</sup>Institute for Research in Biomedicine (IRB Barcelona), Barcelona Institute of Science and Technology; Barcelona, 08028, Spain.

<sup>10</sup>Pediatric Cancer Center Barcelona (PCCB), Hospital Sant Joan de Déu; Esplugues de Llobregat (Barcelona), 08950, Spain.

<sup>11</sup>Institució Catalana de Recerca i Estudis Avançats (ICREA); Barcelona, 08010, Spain.

<sup>‡</sup>These authors contributed equally to this work.

\*Corresponding author. Email: sara.sanchezm@sjd.es (S.S-M.); jaume.mora@sjd.es (J.M.)

<sup>†</sup>These authors contributed equally to this work as co-senior authors.

## 8 **Abstract**

9 Ewing Sarcoma (EwS) is an aggressive bone and soft tissue tumor driven by the fusion  
10 oncoprotein EWSR1-FLI1. This aberrant transcription factor binds to GGAA  
11 microsatellites, causing epigenetic reprogramming through the formation of active neo-  
12 enhancers in a permissive cellular context. Inhibition of the oncogene remains  
13 challenging and current efforts seek to exploit emergent epigenetic treatments targeting  
14 EWSR1-FLI1 cofactors. Here, stemming from the genome-wide redistribution of  
15 H3K27me3 upon expression of EWSR1-FLI1 in human pediatric mesenchymal stem  
16 cells (hpMSC), we unravel the contribution of the H3K27me3 demethylases  
17 KDM6A/UTX and KDM6B/JMJD3 in transcriptional activation at EWSR1-FLI1  
18 enhancers. We found that KDM6A has a demethylase-independent role in recruiting  
19 BRG1 at EWSR1-FLI1-primed enhancers containing single GGAA motifs, which is  
20 critical for EwS tumor growth. Conversely, KDM6B demethylates H3K27me3 at specific  
21 EWSR1-FLI1-active enhancers and co-localizes with BRG1 at GGAA repeats. KDM6B  
22 knockout impairs tumor growth and its deletion synergizes with EZH2 inhibitors. Our  
23 results highlight KDM6 demethylases as EWSR1-FLI1 **functional partners** with potential  
24 for future targeted strategies.

## 25 **Teaser**

26 **Unveiling KDM6 demethylases as key players in Ewing sarcoma.**

## 27 **Introduction**

28 Ewing Sarcoma (EwS) is a deadly neoplasm that arises in the bones and soft tissues of  
29 children, adolescents and young adults (1). Whole-genome sequencing studies of EwS  
30 tumors reported a remarkably genome stability with very low mutational burden (2, 3).  
31 Like many developmental cancers, EwS is characterized by a differentiation block during  
32 development conferred by the expression of an oncogenic driver (4). The characteristic  
33 reciprocal chromosomal translocation most commonly involves the *EWSR1 RNA-binding*  
34 *protein 1 (EWSR1)* gene in chromosome 11 and the *ETS transcription factor family*  
35 *member Fli-1 proto-oncogene (FLI1)* in chromosome 22 (5). The resulting fusion protein  
36 retains the transactivation domain of *EWSR1* fused to the DNA-binding domain of *FLI1*  
37 and acts as an aberrant transcription factor (6, 7). However, EWSR1-FLI1 can only  
38 achieve oncogenic transformation in the right cellular background (8-10). While EWSR1-  
39 FLI1 induces growth arrest or apoptosis in differentiated primary cells (11, 12), its  
40 expression in human mesenchymal stem cells (hMSC) recapitulates the EwS gene  
41 signature (9, 13). Nevertheless, stronger induction of oncogenic targets occurs in human  
42 pediatric MSC (hpMSC) as opposed to adult derived mesenchymal cells which highlights  
43 the need for a permissive molecular framework (13).

44 EWSR1-FLI1 exhibits a high affinity to bind DNA through GGAA motifs, a class of ETS  
45 specific response element, activating or repressing their targets based upon the number of  
46 motif repeats (14, 15). At GGAA repeats, multimers of EWSR1-FLI1 establish *de novo*  
47 active enhancers (neo-enhancers) by promoting chromatin opening through recruitment  
48 of chromatin-modifying complexes. Indeed, in EwS cell lines and primary tumors the  
49 vast majority of EWSR1-FLI1 binding sites are decorated by H3K27ac, a post-  
50 translational histone mark associated to active enhancers (16, 17). Consistently, EWSR1-  
51 FLI1 features scaffolding properties and recruits core members of the transcriptional

52 activator mammalian SWItch/Sucrose Non-Fermentable (SWI/SNF) chromatin or  
53 BRG1/BRM-associated factor (BAF) complex, such as BAF155, at GGAA repeats that  
54 are critical for transcriptional activation (18). Furthermore, we have described that  
55 RING1B, a member of the Polycomb group (PcG) family of proteins (19), facilitates  
56 EWSR1-FLI1 recruitment towards key enhancers (20). Although the mechanism behind  
57 EWSR1-FLI1 gene repression is less well understood, it has been proposed that binding  
58 of EWSR1-FLI1 monomers on single instances of the GGAA motifs causes displacement  
59 of endogenous ETS transcription factors decreasing transcriptional activation (16).  
60 Besides, a large number of transcriptional repressors such as *NKX2-2* are induced by  
61 EWSR1-FLI1, highlighting indirect mechanisms to mediate gene silencing (21).  
62 The post-translational histone mark trimethylation of H3K27 (H3K27me<sub>3</sub>) decorates  
63 promoters and enhancers of repressed and bivalent genes (22). H3K27me<sub>3</sub> mark restricts  
64 cell fate by limiting chromatin accessibility to key developmental genes, thus proper  
65 deposition or removal of this mark in a timely manner is critical during development (23).  
66 EZH2, the core member of the Polycomb Repressive Complex 2 (PRC2), is the primary  
67 enzymatic writer of H3K27me<sub>3</sub> that maintains the silencing patterning fundamental for  
68 cell identity and proper differentiation (24, 25). Removal of H3K27me<sub>3</sub> concerted with  
69 promoter activation is mediated by members of the KDM6 family of demethylases,  
70 including KDM6A (UTX) and KDM6B (JMJD3), through its JmjC domain (26, 27), and  
71 determine specification of human neural progenitor cells (28). KDM6A has been  
72 described as a partner of the Set1/MLL complex which is responsible for active gene  
73 expression by methylation of H3K4 at active enhancers (29, 30), while KDM6B has been  
74 reported to cooperate with the transcription factor KLF4 in enhancer-driven  
75 reprogramming and with SMAD3 in neural specific enhancers (31, 32).

76 Deregulation of the H3K27me3 balance that is governed by the coordinated enzymatic  
77 activities of EZH2 and KDM6A/KDM6B leads to differentiation defects and cancer (33).  
78 EZH2 has been involved in the tumor progression mechanisms of a variety of cancer  
79 types (34), while KDM6A and KDM6B have been identified in numerous malignancies  
80 with either oncogenic or tumor suppressor roles (35-39). We previously demonstrated  
81 that EWSR1-FLI1 occupies weak repressed Polycomb chromatin states in hMSC (20).  
82 Although EWSR1-FLI1-bound GGAA repeats are devoid of H3K27me3 both in EwS cell  
83 lines and primary tumors (16, 17), in Human Umbilical Vein Endothelial Cells  
84 (HUVECs) and hpMSC these regions are extensively decorated with H3K27me3 (8, 40).  
85 EZH2 is a well-known directly activated target by EWSR1-FLI1 that blocks  
86 neuroectodermal and endothelial differentiation in EwS (9, 41). However, the precise  
87 mechanism behind the equilibrium of H3K27me3 deposition and removal and its impact  
88 in EwS tumor development have not yet been addressed.

89 Here, we shed light on the dynamics of H3K27me3 removal by KDM6A and KDM6B  
90 demethylases within the context of EwS. First, we show how H3K27me3 is redistributed  
91 genome-wide during EwS tumorigenesis in hpMSCs. Next, we demonstrate that KDM6A  
92 and KDM6B bind to the same genomic regions as EWSR1-FLI1, with KDM6A  
93 decorating EWSR1-FLI1 primed enhancers containing GGAA single motifs and KDM6B  
94 characteristically enriched at active enhancers containing multimeric GGAA repeats.  
95 Importantly, both KDM6A and KDM6B demethylases are involved in EWSR1-FLI1-  
96 related transcriptional activation in a demethylase-independent and dependent manner,  
97 respectively, being critical for EwS tumor growth. Our findings provide deep knowledge  
98 regarding specific functions of H3K27me3 KDM6 demethylases in EwS and support  
99 epigenetic treatment strategies based upon the reversibility of the processes involved in  
100 the H3K27me3 equilibrium.

101 **Results**

102 **H3K27me3 genome-wide redistribution upon EWSR1-FLI1 overexpression in**  
103 **hpMSCs**

104 Several groups have documented a *bona fide* list of GGAA repeats bound by EWSR1-  
105 FLI1 to activate transcription (15, 16, 42). Recently, our group and others have  
106 demonstrated that overexpression of the oncogene triggers a loss of H3K27me3 at  
107 promoters of genes that become transcriptionally activated in HUVEC cells and neural  
108 crest stem cells (NCSC) (20, 43). In an attempt to determine the global extension of such  
109 a decrease in H3K27me3, we analyzed published ChIP-seq data on H3K27me3 in hpMSC  
110 overexpressing the fusion oncogene (40). We first examined the distribution of  
111 H3K27me3 in genes decorated by this mark in the hpMSC control condition (5 kb around  
112 TSS) and revealed a maximal decrease at 2 kb upstream the TSS upon EWSR1-FLI1  
113 overexpression, concomitant with an increase in H3K27ac specific for TSS (fig. S1A).  
114 Nevertheless, Western blot analysis reported similar H3K27me3 levels in both conditions  
115 (Fig. 1A), suggesting an overall genome-wide redistribution following the introduction  
116 of EWSR1-FLI1. In order to confirm this hypothesis, we segmented the genome into  
117 3,069,655 bins of 1 kb and determined that averaged H3K27me3 signal strength along  
118 bins was highly correlated between control and EWSR1-FLI1 samples confirming the  
119 redistribution of this mark (fig. S1B). Specifically, we identified 103,766 bins with a  
120 significant reduction of H3K27me3 (Down bins) and 110,845 bins with a significant gain  
121 of H3K27me3 (Up bins) upon EWSR1-FLI1 overexpression (fig. S1C). Of note, as  
122 previously proposed (20), most genomic regions presenting H3K27me3 down bins upon  
123 expression of EWSR1-FLI1 in hpMSC are notably enriched over regulatory sequences of  
124 bivalent genes (fig. S1D). Integration of H3K27me3 data with ChIP-seq data for EWSR1-  
125 FLI1 reveals 67,224 bins where the oncogene was enriched. Importantly, we observed a

126 progressive loss of H3K27me3 along with a gain of the EWSR1-FLI1 signal in a fraction  
127 of 4,080 overlapping bins upon EWSR1-FLI1 overexpression (Fig. 1B). To test whether  
128 H3K27me3 redistribution occurs at the gene level, we searched for those genes in which  
129 the gain/loss was significant (FC2, min>0.01; 2175 genes down and 2289 genes up) (Fig.  
130 1C). Functional analysis of genes losing H3K27me3 correlated with neural processes and  
131 metabolism (fig. S1E and table S1). For instance, *NKX2-2*, a well-known EWSR1-FLI1  
132 target, exhibited a gain of H3K27ac with a concomitant moderate H3K27me3 decay along  
133 its promoter and regulating enhancers (Fig. 1D). Association with the TGF-beta receptor  
134 signaling pathway was obtained for genes gaining H3K27me3 (fig. S1E and table S1), in  
135 agreement with the well-known repressed state of genes from this pathway in EwS (44).  
136 For instance, *TGFBI* was one of the genes in which a gain of H3K27me3 after EWSR1-  
137 FLI1 introduction was observed along the gene body (Fig. 1E). Altogether, these results  
138 demonstrate that EWSR1-FLI1 targets regions decorated with H3K27me3 promoting its  
139 redistribution.

140 Next, we hypothesized that KDM6A and KDM6B, which are the enzymes responsible  
141 for the demethylation of H3K27me3 (26, 27), might be implicated in the loss of  
142 H3K27me3 at promoters and enhancers of EWSR1-FLI1 targets. Indeed, when evaluating  
143 the expression of KDM6A and KDM6B demethylases in a panel of cancer cell lines (45),  
144 we found that while KDM6A expression was similar across tumor types, KDM6B was  
145 more expressed in EwS cell lines than in other sarcomas (Fig. 1F). Similar trends were  
146 reported in 184 EwS tumors at diagnosis (GSE17679, GSE34620 and GSE37371  
147 accessions), where we confirmed that the expression of both KDM6A and KDM6B is  
148 consistently higher than in MSC, while KDM6B expression in EwS tumors was  
149 particularly high compared to other sarcomas (Fig. 1G). Analysis of KDM6A and  
150 KDM6B by immunohistochemistry in 43 EwS primary tumor specimens from newly

151 diagnosed patients from our institution revealed that both demethylases were highly  
152 expressed by semi-quantitative histoscore (H-score) analysis (Fig. 1H and fig. S1F). No  
153 correlation between KDM6A and KDM6B expression in EwS tumors was found  
154 according to the statistical analysis of their H-score (fig. S1G). Taken together, gene  
155 expression data and immunohistochemical studies indicate that KDM6A and KDM6B are  
156 highly expressed in EwS cell lines and in primary tumor samples.

157 **KDM6A and KDM6B co-localize genome-wide with EWSR1-FLI1 at primed and**  
158 **active enhancers**

159 To shed light on whether KDM6A and KDM6B demethylases are involved in H3K27me3  
160 to H3K27ac switches in enhancers regulated by EWSR1-FLI1, we carried out chromatin  
161 immunoprecipitation followed by high-throughput sequencing (ChIP-seq) for KDM6A,  
162 KDM6B and EWSR1-FLI1 in the EwS cell line A673. We identified 3,737 peaks for  
163 KDM6A, 2,687 for KDM6B, and 4,800 for EWSR1-FLI1 (P value < 0.05 in all cases;  
164 FDR < 10<sup>-3</sup> for KDM6A and EWSR1-FLI1, FDR < 10<sup>-5</sup> for KDM6B) (fig. S2A and table  
165 S2). At the genomic level, we observed a clear preference for intergenic and genic regions  
166 in all cases (Fig. 2A), which indicates a role at enhancers as previously described (29,  
167 31). KDM6B peaks were enriched at promoter regions (10.1%), compared to EWSR1-  
168 FLI1 and KDM6A peaks. We next categorized KDM6A, KDM6B and EWSR1-FLI1  
169 peaks into active, primed or poised enhancers, and in active or poised promoters based  
170 on Blanco *et al.* (46). Primed enhancers are regulatory regions that correlate with the  
171 H3K4me1 mark in absence of H3K27ac (47). Remarkably, KDM6A is more abundant at  
172 primed enhancers, whereas KDM6B mimics EWR1-FLI1 distribution and mainly  
173 associates to active enhancers (Fig. 2B). In agreement with this, motif analysis found the  
174 characteristic single instance of the GGAA consensus on KDM6A sites, while KDM6B  
175 and EWR1-FLI1 peaks were enriched in both multiple and single GGAA motifs (fig.



176 S2B). Gene association to peaks retrieved 1,511 genes for KDM6A and 1,207 genes for  
177 KDM6B, that were enriched in axon guidance, axonogenesis or nervous system  
178 development GO categories for both demethylases (fig. S2C and table S3), indicating an  
179 important role of these demethylases in promoting neuronal differentiation as previously  
180 described (28). Primed enhancers define a state prior to activation that does not yield  
181 RNA and correlates with cell type specificity (47, 48). Thus, the enrichment of KDM6A  
182 in primed enhancers supports the involvement of this enzyme in neural cell specification.  
183 Strikingly, when intersecting KDM6A and KDM6B peaks with the set of 697 EWSR1-  
184 FLI1-superenhancers defined by Tomazou *et al.* (17), we found an overlap of 23% and  
185 35%, respectively. To elucidate to which extent KDM6A and KDM6B co-localize with  
186 EWSR1-FLI1, we intersected peaks from the three entities and found a strong overlap of  
187 EWSR1-FLI1 with both demethylases (A-B-EF group) and with each demethylase  
188 separately (A-EF and B-EF) (Fig. 2C). This result was validated in another EwS cell line,  
189 TC71, where we found 1163 common peaks between EWSR1-FLI1 and  
190 KDM6A/KDM6B (P value < 0.05; FDR < 10<sup>-5</sup> in all cases) (fig. S2D). **Of note, ChIP-seq**  
191 **for EZH2 retrieves no intersection with EWSR1-FLI1 (fig. S2E), in agreement with**  
192 **previous studies (16, 20).** Motif analysis in A673 cell line revealed a strong enrichment  
193 in GGAA multimeric repeats when EWSR1-FLI1 stands alone or together with KDM6B  
194 (B-EF group), while the presence of KDM6A is linked to the single GGAA motif (A-B-  
195 EF and A-EF groups), suggesting that KDM6A partners with a unique set of EWSR1-  
196 FLI1 peaks (Fig. 2C). In agreement with our motif characterization, KDM6B together  
197 with EWSR1-FLI1 (B-EF group) strongly overlap with high levels of H3K27ac and  
198 H3K4me1 (i.e. active enhancers), while KDM6A is associated to lower levels of  
199 H3K27ac and enrichment in H3K4me1 (i.e. primed enhancers) (Fig. 2, D and E).  
200 Remarkably, KDM6B alone was found in a subset of transcriptionally active promoters

201 (H3K4me3 and H3K27ac) (Fig. 2E and fig. S2F), suggesting differential functionalities  
202 for each demethylase. No significant enrichment of H3K27me3 was found in any  
203 collection of peaks (fig. S2F). Previously we described RING1B co-localization genome-  
204 wide with EWSR1-FLI1 at active enhancers of key target genes (20). Interestingly,  
205 RING1B is enriched both in EWSR1-FLI1 enhancers containing KDM6A and KDM6B  
206 (B-EF, A-EF and A-B-EF group (fig. S2G). Overall, our data support three classes of  
207 enhancers according to their composition: (i) those where KDM6A and KDM6B co-  
208 localize with the oncogene (A-B-EF) at single GGAA motifs (e.g. *CDH11* gene, Fig. 2F  
209 and fig. S2I), (ii) KDM6A/EWSR1-FLI1 enhancers (A-EF) containing single GGAA  
210 motifs (e.g. *SMYD3*, fig. S2H); and (iii) those containing the overlap of KDM6B and  
211 EWSR1-FLI1 (without KDM6A, B-EF) and enrichment at multimeric GGAA repeats  
212 (e.g. *NKX2-2* enhancer, Fig. 2F and fig. S2I). Altogether, the differential location and  
213 partnership identified for each of the KDM6 demethylases in EwS suggest that KDM6B  
214 specifies EWSR1-FLI1 for the most active regions and KDM6A signals for a specific set  
215 of enhancers that commit to neural lineage.

## 216 **Knockdown of KDM6A and KDM6B downregulates EWSR1-FLI1-activated** 217 **targets**

218 To understand whether EWSR1-FLI1 changes the distribution of KDM6A and KDM6B  
219 on chromatin, we performed KDM6A and KDM6B ChIP-seq in a HeLa cell model that  
220 express EWSR1-FLI1 under the control of a doxycycline-inducible promoter (49). As  
221 shown in Fig. 3A and 3B, although KDM6A and KDM6B are already present in EWSR1-  
222 FLI1 bound positions before induction, both demethylases increase their enrichment at  
223 these positions once the oncogene is overexpressed. These data suggest EWSR1-FLI1  
224 might be able to cause changes in the genome-wide occupancy for these demethylases.  
225 Our previous results suggested two different classes of EWSR1-FLI1 induced neo-

226 enhancers, when partnered with KDM6A -primed enhancers- or with KDM6B -active  
227 enhancers-. Indeed, the expression of genes in the proximity of enhancers containing  
228 KDM6A is lower than those with KDM6B (Fig. 3C). To gain insight into the role of both  
229 demethylases on the EWSR1-FLI1-transactivation activity, we knocked-down KDM6A  
230 and KDM6B in two EwS cell lines using a doxycycline-inducible system. We reported  
231 the knockdown of the demethylases at the protein level with two different shRNA  
232 sequences (KDM6A sh#1 and sh#2; KDM6B sh#1 and sh#2) in both A673 and TC71  
233 cells (Fig. 3D and fig. S3A). In order to study genome-wide expression changes we  
234 carried out global transcriptome analysis by RNA-seq upon knockdown of KDM6A (sh#1  
235 and sh#2) and KDM6B (sh#1 and sh#2). Loss of each demethylase resulted in gene  
236 downregulation in A673 ( $P_{adj} < 0.01$  and log FC cut-off 0.5 and FPKM  $> 10$ , fig. S3B,  
237 fig. S3C and table S4) and TC71 cell lines ( $P_{adj} < 0.1$  and log FC cut-off 0.32 and FPKM  
238  $> 5$ , fig. S3C). Gene Set Enrichment Analysis (GSEA) in the A673 cell line found that  
239 both KDM6A and KDM6B are necessary for the activation of Epithelial-to-Mesenchymal  
240 Transition (EMT) genes (Fig. 3E and table S4). However, there is little overlap between  
241 both sets of deregulated genes upon demethylase knockdown (86 up-regulated and 34  
242 down-regulated genes in common between KDM6A and KDM6B), confirming different  
243 functionalities for each demethylase. All these results support a selective active role of  
244 KDM6A and KDM6B in the transcriptional activation network necessary for EwS  
245 tumorigenesis.

246 To further understand the relevance of KDM6A and KDM6B in the transcriptional  
247 activation program of EWSR1-FLI1, we intersected genes associated to the genomic  
248 regions where these demethylases and EWSR1-FLI1 co-localize with deregulated targets  
249 in A673. To associate genes to peaks we captured every gene in a distance of 100 kb of  
250 both combinations of ChIP-seq peaks and obtained 3,134 genes and 3,326 genes in the

251 vicinity of EWSR1-FLI1/KDM6A and EWSR1-FLI1/KDM6B, respectively. We then  
252 intersected these direct targets with the set of KDM6A and KDM6B significantly  
253 downregulated or upregulated genes. We obtained 64 directly activated targets for  
254 KDM6A and 139 for KDM6B with EWSR1-FLI1 peak (Fig. 3F and table S4), while 20  
255 directly repressed targets for KDM6A and 101 for KDM6B were identified (fig. S3D).  
256 GO analysis of activated-targets reported neural categories such as axonogenesis,  
257 previously observed in figure S2C, and cell migration (fig. S3E). Among the list of  
258 KDM6A/EWSR1-FLI1 activated targets we found *CDH11*, *IRS2* and *SYT1* (Fig. 3, F and  
259 G and fig. S3F); while for KDM6B/EWSR1-FLI1 we found targets such as *IGF1*, *MMP9*  
260 and *JARID2* previously described in EwS (Fig. 3, F and H and fig. S3G). Interestingly,  
261 most of the direct targets of KDM6A contain peak for KDM6B although only few targets  
262 were commonly downregulated. These results support the differential role of KDM6A  
263 and KDM6B in transcriptional activation in EwS.

#### 264 **KDM6A recruits BRG1 to EWSR1-FLI1-activated enhancers in a demethylase-** 265 **independent manner**

266 In order to avoid off-target effects and induce a permanent gene modification, we  
267 generated knock-outs (KO) of KDM6 using CRISPR methodology. We confirmed that  
268 our KO completely abolished KDM6A expression in A673 cells without causing changes  
269 in EWSR1-FLI1 and KDM6B levels (Fig. 4A). Despite loss of the demethylase enzymatic  
270 activity, global levels of H3K27me3 as well as H3K4me1 and H3K27ac were not altered  
271 upon KO in A673 (fig. S4A). Further characterization of KDM6A KO by RNA-seq  
272 showed that the percentage of downregulated genes (activated targets, 69.1 and 67.1%,  
273 for sgRNA#1 and #2, respectively) was higher than for upregulated genes (repressed  
274 targets, 30.9 and 32.9%, for sgRNA#1 and #2, respectively) (fig. S4B), supporting the  
275 transcriptional activation role of KDM6A. Indeed, activated genes were enriched in

276 axonogenesis categories (fig. S4B) as already observed with shRNA (fig. S3E).  
277 **Intersection of KDM6A-EWSR1-FLI1 ChIP-seq direct targets (distance of 100 kb) with**  
278 **significantly decreased targets for KDM6A KO, confirmed 260 direct activated targets (P**  
279 **adj < 0.05 and log FC cut-off 1, Fig. 4B, Table S5).** We further validated by RT-qPCR  
280 the downregulation of genes containing KDM6A and EWSR1-FLI1 with KDM6B (A-B-  
281 EF group), while the expression of targets containing KDM6B and EWSR1-FLI1 (B-EF  
282 group) remained unchanged (Fig. 4C). The decrease in gene expression of KDM6A-  
283 EWSR1-FLI1 targets identified by ChIP-seq (fig. S2D), was confirmed in a second EwS  
284 cell line, TC71, upon KDM6A KO (fig. S4, C and D).

285 To elucidate genome wide the contribution of KDM6A demethylase activity in the  
286 decreased expression of defined targets, **we performed H3K27me3 ChIP-seq normalized**  
287 **with spike-in** in A673 control and KDM6A KO (sgCTRL and sgKDM6A A673 cells,  
288 respectively). The resulting H3K27me3 peaks were divided into three classes: (i)  
289 commonly found in control and KDM6A KO, (ii) only found in the control condition,  
290 and (iii) only found in KDM6A KO. **Quantification of signal strength for each class of**  
291 **peaks showed no changes in the common group (sgCTRL+/sgKDM6A+), while a new**  
292 **group of 1,616 peaks emerge upon deletion of the demethylase (sgCTRL-/sgKDM6A+,**  
293 **Fig. 4D).** Those regions gaining H3K27me3 upon KDM6A KO associated with 299 genes  
294 (Fig. 4E). However, **the average profile of H3K27me3 around the TSS of KDM6A-**  
295 **activated genes (downregulated upon KDM6A KO) revealed no correlation between**  
296 **changes on their gene expression and H3K27me3 levels** (fig. S4E), exemplified with  
297 *SYTI* in Figure 4F. To more accurately pinpoint the regions of the genome presenting  
298 higher H3K27me3 changes, we segmented the genome in bins of 1 kb and determined  
299 the average signal strength of the ChIP-seq for both conditions. This analysis retrieved  
300 **579,992 bins** gaining (up) H3K27me3 and **142,556 bins** losing H3K27me3 (down) (fig.

301 S4, F and G), supporting a general redistribution of the mark already observed by other  
302 authors (50).

303 KDM6A demethylase-independent functions have been proposed in the Kabuki  
304 syndrome, in the context of cell-induced differentiation with retinoic acid, mesoderm  
305 differentiation of embryonic stem cells and in lung cancer (30, 37, 51, 52). To analyze  
306 the contribution of KDM6A demethylase activity at KDM6A-EWSR1-FLI1 targets we  
307 reintroduced KDM6A WT or a dead mutant enzyme (mutations in H1146A and E1148A)  
308 in KDM6A KO cells (53). As shown in Figure 4G, both WT and dead mutant enzymes  
309 recovered the expression on KDM6A-EWSR1-FLI1 target genes (*SYT1*, *IRS2*, *CDH11*  
310 and *PCSK2*) confirming that the transcriptional activating function of KDM6A is  
311 independent of its demethylase activity. This recovery of expression was also observed  
312 in genes where only KDM6A is present with the oncogene, such as *CDH6* and *TCF7L1*  
313 (Fig. 4G).

314 KDM6A has been described to physically associate with the BAF complex member  
315 BRG1/SMARCA4 (54-56), which constitutes the central catalytic subunit that uses the  
316 energy derived from ATP-hydrolysis to remodel nucleosomes and regulate transcription  
317 (57). To elucidate whether KDM6A was mediating transcriptional activation at enhancers  
318 through the recruitment of BRG1, first we evaluated whether they physically associate.  
319 Using co-immunoprecipitation we observed that indeed, both proteins interact (Fig.  
320 S4H). Next we evaluated BRG1 enrichment genome wide by ChIP-seq and observed that  
321 intersection of KDM6A-EWSR1/FLI1 with BRG1 retrieved 1,808 common regions (Fig.  
322 4H). Although peak signal intensity was unmodified in the global set of BRG1 peaks  
323 upon KDM6A KO (fig. S4I), ChIP-seq signal significantly decreases for the common  
324 BRG1-KDM6A regions (Fig. 4I). Validation of genome-wide results by ChIP-qPCR  
325 showed that H3K27me3 levels were unmodified upon KDM6A KO at the enhancer and

326 promoter regions of two EWSR1-FLI1/KDM6A-activated target genes, *IRS2* and *SYT1*,  
327 both in A673 and TC71 cell lines (Fig. 4J and fig. S4J), while BRG1 was evicted from  
328 enhancer regions following KDM6A deletion (Fig. 4J). These results were also confirmed  
329 upon KDM6A knockdown in the A673 cell line (fig. S4K). Altogether, our results suggest  
330 that KDM6A contributes to the recruitment of BRG1 at EWSR1-FLI1 activated  
331 enhancers facilitating transcriptional activation through a demethylase-independent  
332 mechanism.

### 333 **KDM6A knockout decreases EwS tumor growth**

334 Based on the previous results where we showed KDM6A being actively collaborating  
335 with EWSR1-FLI1 at enhancers, we aimed to investigate the dependency of EwS tumor  
336 formation on KDM6A. First, to determine whether KDM6A affects EwS cell growth, we  
337 studied cell proliferation *in vitro* of KDM6A KO cells. We observed a decrease of cell  
338 proliferation on days 3 and 6 for both sgKDM6A#1 and #2 KO A673 cells (fig. S5A).  
339 Moreover, KDM6A KO cells exhibited a significant decrease in their clonogenic capacity  
340 compared to control and parental cells (Fig. 5A and fig. S5B). Next, we subcutaneously  
341 injected sgCTRL and sgKDM6A #1 and #2 KO A673 cells into athymic nude mice and  
342 monitored tumor growth. Xenografts of parental cells were included as an additional  
343 control for tumor growth. Interestingly, we found KDM6A KO (#1 and #2) showed a  
344 delay in tumor growth compared to control and parental-derived tumors (Fig. 5B and fig.  
345 S5C). At 17 days post-injection tumors were significantly smaller for sgKDM6A#1  
346 (mean tumor volume of 121 for sgKDM6A#1 and 252.5 and 280mm<sup>3</sup> for A673 and  
347 sgCTRL tumors, respectively) (fig. S5D). We confirmed downregulation of KDM6A by  
348 RT-qPCR and Western Blot (Fig. 5C and fig. S5E). Moreover, median survival increased  
349 from 25 (control) to 35 days for sgKDM6A#1 and from 20.5 (control) to 55 days for  
350 sgKDM6A#2, respectively (Fig. 5D). Tumor engraftment was significantly delayed in

351 both KDM6A KO clones, with a median tumor engraftment of 20 days for sgKDM6A#1  
352 compared to 16 days for sgCTRL and parental tumors (Fig. 5E). Importantly, we  
353 confirmed a decreased expression of enhancer-bound KDM6A/EWSR1-FLI1 targets,  
354 *CDH11* and *IRS2* (Fig. 5C), in xenografted tumors, supporting the transcriptional  
355 activating role of KDM6A at these oncogenic targets. Immunohistochemical analysis of  
356 tumors confirmed the expression of the EwS marker CD99 and significantly lower  
357 expression of the proliferation marker Ki-67 in sgKDM6A-derived tumors (Fig. 5F and  
358 fig. S5F and G). **The delay in tumor growth and the increase in survival compared to**  
359 **control were also** observed when TC71 cells containing sgKDM6A #1 and #2 were used  
360 (fig. S5H **and S5I**). All these results confirm KDM6A as a critical factor for EwS tumor  
361 growth.

362 Previously, we found KDM6A targets enriched in categories related to neural  
363 differentiation (fig. S3D). Neurofilament (NF) proteins are cytoskeleton proteins that  
364 maintain neural axons and dendrites (58). Neoplastic cells of neural origin or those  
365 exhibiting neural differentiation express NF. EwS tumors show positivity to cell surface  
366 antigens related to neuroectodermal lineage (59) and intracellular markers such as neuron  
367 specific enolase (NSE) and NF proteins (60, 61). The heavy chain of neurofilament  
368 protein NF200 is highly expressed in EwS cells and tumors (62, 63). Considering that  
369 KDM6A targets developmental neural pathways in EwS, we hypothesized that neural  
370 markers such as NF200 could be perturbed in KDM6A-KO tumors. Indeed, NF200 is  
371 highly expressed in publicly available datasets of EwS tumors and cell lines (fig. **S5, J**  
372 **and K**). Furthermore, immunohistochemical analysis revealed lower levels of NF200 in  
373 KDM6A-KO tumors as compared with those from control group (Fig. 5F). Altogether,  
374 our data indicate KDM6A exerts its critical role on EwS tumor growth and engraftment  
375 likely regulating neural pathways *in vivo*.



## 376 **Impact of KDM6B knockout in EWSR1-FLI1 targets**

377 KDM6A and KDM6B in conjunction with EWSR1-FLI1 participate at enhancers of  
378 neural genes with a different configuration of GGAA motifs, suggesting that both  
379 demethylases do not necessarily play the same function in EwS. To understand whether  
380 the role of KDM6B in EwS cells is associated with its demethylase activity, we  
381 investigated the H3K27me3 dynamics in KDM6B depleted cells. First, we confirmed the  
382 KO of KDM6B in A673 cells, while levels of EWSR1-FLI1 and KDM6A remained  
383 unchanged (Fig. 6A). Next, we evaluated the levels of H3K27me3 by Western blot in  
384 KDM6B KO. We found that the depletion of the demethylase did not alter the global  
385 levels of H3K27me3 (fig. S6A). Further characterization of KDM6B KO by RNA-seq  
386 retrieved higher percentages of downregulated genes (32.1 and 71.7%, activated targets)  
387 than upregulated genes (17.9 and 28.3%, repressed targets) for sgRNA#1 and #2,  
388 respectively (fig. S6B). As previously shown for KDM6B, activated genes were enriched  
389 in cell migration (fig. S6B). By intersecting **KDM6B-EWSR1-FLI1 ChIP-seq direct**  
390 **targets (distance of 100 kb)** with significantly decreased targets for KDM6B KO, we  
391 defined 49 direct activated targets ( $P_{adj} < 0.05$  and log FC cut-off 0.5, Fig. 6B, **Table**  
392 **S5**). We confirmed by RT-qPCR that expression of targets potentially regulated by  
393 enhancers containing KDM6B and EWSR1-FLI1 (B-EF group) was exclusively  
394 dependent on KDM6B, while KDM6B KO did not affect expression of targets containing  
395 enhancers with KDM6A binding sites (A-B-EF group, Fig. 6C). Decreased expression in  
396 KDM6B and EWSR1-FLI1 targets inspected by ChIP-seq (fig. S2D), upon KDM6B KO  
397 was confirmed in a second cell line, TC71 (fig. S6C and D). To inspect for the  
398 demethylase activity of KDM6B genome wide, we performed **H3K27me3 ChIP-seq**  
399 **normalized with spike-in** in A673 control and KDM6B KO (sgCTRL and sgKDM6B,  
400 respectively). The obtained peaks were divided in three groups, as previously described

401 for KDM6A. Interestingly, in this case, we observed a decrease in the peaks from  
402 common group (sgCTRL+/sgKDM6B+ group), which are repressed regions maintained  
403 between both conditions. Although unexpected, these results are in concordance with the  
404 decrease in EZH2 expression observed upon KDM6B KO (Fig. 6C). As shown in Figure  
405 6D, H3K27me3 was increased in 2,366 peaks from the sgCTRL-/sgKDM6B+ group,  
406 corresponding to 400 genes (Fig. 6E), while the average profile of H3K27me3 around the  
407 TSS of KDM6B activated genes (downregulated upon KDM6B KO) showed no  
408 correlation between changes on their gene expression and H3K27me3 levels (fig. S6E).  
409 The intersection of the set of 400 genes gaining H3K27me3 with those gaining the  
410 repressive mark upon KDM6A retrieves a minimal 5% of intersection, supporting the  
411 differential contribution of each demethylase. Bin analysis of H3K27me3 in both  
412 samples (sgCTRL and sgKDM6B#2) retrieves 380,371 bins gaining and 442,200 losing  
413 H3K27me3, suggesting a redistribution of the repressive mark (fig. S6, F and G).  
414 Although changes in expression did not correlate with increase of H3K27me3 at TSS  
415 upon KDM6B KO, we observed moderate recoveries of the H3K27me3 levels genome-  
416 wide at specific EWSR1/FLI1-KDM6B enhancers (Fig. 6F), whereas mild enrichment of  
417 the repressive mark at these specific regions was validated by ChIP-qPCR (Fig. 6G).  
418 Moreover, when we treated EwS cells with the KDM6A/B demethylase inhibitor GSK-  
419 J4, we found that the expression of EWSR1-FLI1-activated targets was decreased  
420 strongly in those targets containing only KDM6B, suggesting that GSK-J4 phenocopies  
421 expression changes induced by KDM6B deletion (fig. S6H). In accordance with  
422 published data describing BAF complex enrichment at GGAA repeats, we show  
423 KDM6B-EWSR1-FLI1 co-localization with the BRG1 subunit (Fig. 6H), which is  
424 enriched in both single and repeat GGAA and co-immunoprecipitated with KDM6B (fig.  
425 S6, I and J). Overall, our results confirm KDM6B exerts its function as demethylase at

426 specific KDM6B/EWSR1-FLI1 targets, while genome-wide changes in H3K27me3 are  
427 counterbalanced by EZH2 drop in KDM6B depleted cells.

428 **KDM6B knockout decreases tumor growth and sensitizes EwS cells to the EZH2**  
429 **inhibitor GSK126**

430 Since KDM6B KO led to a lower clonogenic capacity of A673 and TC71 EwS cells, it  
431 suggested that the demethylase activity in EWSR1-FLI1 targets could be essential for  
432 tumor growth (Fig. 7A and fig. S7, A, B and C). To assess the relevance of KDM6B in  
433 vivo, we generated xenografts by subcutaneously injecting sgCTRL and sgKDM6B #1  
434 and #2 A673 cells into athymic nude mice. KDM6B KO cells had a slower tumor growth  
435 and an increase in survival from 18.5 days in control to 30 and 33 in sgKDM&B #1 and  
436 #2, respectively (Fig. 7, B and C). Immunohistochemical analysis of tumors confirmed  
437 reduced levels of KDM6B and Ki67 (Fig. 7D).

438 The methyltransferase inhibitor GSK126 has been widely used to epigenetically de-  
439 repress key targets in EwS (64-66). To further elucidate whether depletion of  
440 KDM6A/KDM6B demethylases would prime EwS cells to EZH2 inhibition we analyzed  
441 cell death in KDM6A/KDM6B KO EwS cells upon GSK126 treatment. GSK126  
442 exposure was sufficient to increase apoptosis by Annexin V staining in KDM6B KO cells,  
443 in contrast to KDM6A depletion where cells remained unaltered (fig. S7, D and E).  
444 Furthermore, only KDM6B KO cells treated with the EZH2 inhibitor showed an increase  
445 in cleaved PARP-1 (c-PARP) and the DNA damage marker  $\gamma$ -H2Ax by Western blot,  
446 while H3K27me3 decreased accordingly upon GSK126 treatment in both KOs (Fig. 7E  
447 and fig. S7F). Next, we assessed whether re-expression of WT KDM6B or its catalytic  
448 inactive form (H1390A and E1392) in KDM6B KO cells influenced the induction of  
449 apoptosis by GSK126. The KDM6B dead mutant recover viability even better than the

450 WT, indicating that the sensitization to GSK126 is not demethylase dependent (fig. S7G).  
451 Consistently, we observed that depletion of KDM6B increased the expression of genes  
452 related to double-strand break repair pathways (figure S7H and table S6). These results  
453 would suggest that EZH2 inhibition synergizes with the DNA damage inflicted by  
454 KDM6B depletion in EwS cells.

## 455 Discussion

456 The importance of H3K27me3 redistribution in cancer has previously been reported in  
457 high-grade glioma, lymphoma, and melanoma, concomitant with a gain of function of  
458 EZH2 (67, 68). In this study, we performed an extensive genome-wide study of  
459 H3K27me3 redistribution upon EwS overexpression. Although the maintenance of the  
460 overall levels of H3K27me3 was previously described upon EWSR1-FLI1 knockdown,  
461 published data on H3K27me3 and our results on KDM6 demethylases confirm locus  
462 specific H3K27me3 changes are relevant for the tumorigenic process (40). Our findings  
463 indicate a genome-wide gain of H3K27me3 in relevant genes from EWSR1-FLI1  
464 pathways, supporting the important role of EZH2 in EwS tumorigenesis (9, 41). The lack  
465 of intersection between EZH2 and the oncogene, as already proposed by other groups  
466 (16), suggests an indirect repressor role for this Polycomb subunit. Further research on  
467 this issue should clarify the functional interaction between EZH2 and EWSR1-FLI1  
468 genome-wide. Importantly, we have previously described that EWSR1-FLI1 targets weak  
469 Polycomb regions in hMSC (20). Here, we confirmed a set of regions in hpMSC highly  
470 enriched in H3K27me3 before oncogene expression, where the loss of H3K27me3 is  
471 concomitant to EWSR1-FLI1 binding, supporting the need for a demethylase at these  
472 regions. Altogether, our results refine the understanding of the early steps of EwS  
473 tumorigenesis and the role of the H3K27me3 mark in defining the transformed epigenome  
474 of EwS.

475 We demonstrated that KDM6A and KDM6B promote the oncogenic process set by  
476 EWSR1-FLI1. The depletion of both demethylases reduced the clonogenic capacity and  
477 tumor growth in EwS xenografts. **Importantly, although deletion of KDM6A and**  
478 **KDM6B does not impede generation of neural progenitor cells from hESC (28), double**  
479 **knockout of these demethylases in EwS is not viable, supporting their relevance in the**  
480 **maintenance of the transformed phenotype. In agreement, KDM6A and KDM6B are**  
481 **functional partners of EWSR1-FLI1 at distinct subsets of active enhancers in EwS.**  
482 Moreover, depletion of KDM6A/B alters pathways related to neural development and  
483 correlate to phenotypical expression of genes involved in EMT, which is intimately linked  
484 to the EwS metastatic processes (69). KDM6A has been identified as one of the 299  
485 cancer driver genes in the cancer genome atlas project (TCGA) (70). Its role in cancer  
486 development is cell-context specific, acting as a tumor suppressor or oncogenic factor.  
487 Loss-of-function mutations in KDM6A have been identified in cancers affecting males  
488 across multiple histiotypes, including T-ALL, pancreatic cancer, B-cell lymphoma, and  
489 medulloblastoma (39, 71-73). Conversely, EwS is listed in the 12th position of cancer  
490 malignancies harboring higher mRNA expression of KDM6A (45). Contrary to the dual  
491 role of KDM6A in cancer, KDM6B has been only related to cancer progression and a  
492 specific signature for EMT in lung and breast cancer (74, 75).

493 Most cancer studies deciphering the mechanisms behind KDM6A and KDM6B are based  
494 on independent approaches for each demethylase or enzymatic inhibition by GSK-J4.  
495 Here, we performed a genome-wide analysis of both KDM6A and KDM6B in two EwS  
496 cell lines showing that both proteins co-localize with EWSR1-FLI1. Our study  
497 demonstrates that KDM6A and KDM6B collaborate with EWSR1-FLI1 shaping two  
498 different classes of enhancers that contribute distinctively to the oncogenic process:  
499 KDM6A enhancers, enriched in single instances of the GGAA motif, and KDM6B

500 enhancers, which are characterized by multimeric GGAA repeats (Fig. 7F). Previous  
501 work by Riggi *et al.* (16) described the single GGAA regions as EWSR1-FLI1-repressed  
502 elements where endogenous transcription factors had been displaced by the oncogene.  
503 Nevertheless, these regions are still decorated with low levels of H3K27ac and  
504 transcription, in agreement with our observation of KDM6A linked to primed enhancers.  
505 These type of enhancers constitute an intermediate state between active and repressed  
506 enhancers (47, 48). Indeed, in our study KDM6A-associated genes containing GGAA  
507 single motifs are less transcribed than those enriched with KDM6B. Although these  
508 results might suggest an important role of KDM6A in determination of cell identity,  
509 further analysis of the nature and implications of these primed enhancers and their  
510 differential regulation is needed.

511 It has been shown that the participation of KDM6A in cancer progression is not restricted  
512 to its enzymatic activity but to a demethylase-independent function (37, 76). **Main**  
513 **changes in H3K27me3 upon depletion of KDM6 demethylases have been described by**  
514 **other groups in regions already containing this mark (28, 32, 50, 77). In our study, the**  
515 **maintenance of H3K27me3 in the group of sgCTRL+/sgKDM6A+ peaks, reinforces the**  
516 **KDM6A demethylase independent role. In contrast, the decrease of H3K27me3 observed**  
517 **in the sgCTRL+/sgKDM6B+ group upon KDM6B KO might be due to reduction of**  
518 **EZH2 expression. In agreement with our results, the expected H3K27me3 recovery upon**  
519 **KDM6B inhibition is counterbalanced by the decrease in EZH2 expression in**  
520 **neuroblastoma (50). A new set of peaks for both KDM6A and KDM6B (sgCTRL-**  
521 **/sgKDM6A+ and sgCTR-/sgKDM6B+) was also observed, with no associated changes**  
522 **in gene expression. Further research should be performed to explain their role. Overall,**  
523 **all this data reinforces the differential behavior between both demethylases. Indeed,**  
524 **treatment with the KDM6A/B demethylase inhibitor GSK-J4 has been reported to be**

525 effective at the preclinical level for pediatric cancers like neuroblastoma and diffuse  
526 intrinsic pontine glioma (DIPG) (78, 79). We have reported a mild increase of H3K27me3  
527 at specific EWSR1-FLI1 enhancers upon KDM6B KO that are consistent with the  
528 downregulation of these targets with GSKJ4 that we and others have observed (80).  
529 Moreover, our results suggest that the effects of GSK-J4 described *in vitro* and *in vivo* by  
530 Heisey *et al.* (80), might be due to the specific targeting of the demethylase activity of  
531 KDM6B.

532 KDM6A recruitment of BRG1 was described at cardiac-specific enhancers as a key step  
533 in activation of cardiac developmental programs (56). Our data reveal that KDM6A  
534 recruits BRG1 at EWSR1-FLI1 enhancers in a demethylase-independent manner with  
535 critical consequences on transcriptional activation of these targets (Fig. 7F). **Nevertheless,**  
536 **given that KDM6A is associated with the H3K4 methyltransferase MLL3/4 complex, a**  
537 **reasonable possibility would imply that both might regulate gene expression through**  
538 **coordinated histone modifications (30).** In EwS, BAF155/SMARCC1 subunits of the  
539 BAF complex are recruited by the fusion oncogene at enhancers containing GGAA  
540 repeats to activate transcription (18). Interestingly, we found a strong overlap between  
541 KDM6A and KDM6B with BRG1 at GGAA single motifs and repeats, respectively.  
542 Although the interplay between KDM6B and BAF complex at GGAA repeats remain to  
543 be elucidated, both might work in cooperation to support the strong transcriptional  
544 activation orchestrated at GGAA repeats. Indeed, KDM6A and KDM6B as well as the  
545 oncogene have been recently implicated in phase separation, adding another level of  
546 regulation that might contribute to EWSR1-FLI1 chromatin remodeling (81, 82).  
547 EZH2 sensitization upon KDM6A loss has been mostly described in cancers, including  
548 multiple myeloma, lung cancer and bladder cancer, where KDM6A acts as tumor  
549 suppressor. In such cases, EZH2 inhibition delays tumor onset and induces tumor

550 regression of KDM6A-null cells (83-85). Here, we observed sensitization to EZH2  
551 inhibition in KDM6B-deleted cells. Nevertheless, contrary to the PRC2 amplification  
552 demonstrated in multiple myeloma and bladder cancer upon KDM6A deletion, EZH2  
553 expression decreased upon KDM6B KO and GSKJ4 treatment in EwS cells. In  
554 agreement, we observed a decrease in the peaks from the common group  
555 (sgCTRL+/sgKDM6B+). These results suggest that EwS mechanistically resembles  
556 pediatric cancers like neuroblastoma, where both KDM6B and EZH2 are overexpressed  
557 and constitute druggable targets (50, 86). It has been proposed that PcG proteins promote  
558 survival of EwS cells in hypoxic conditions by repression of *KCNA5* (66). Indeed,  
559 inhibition of EZH2 methyltransferase activity has no impact on cell survival under  
560 physiological conditions but results in loss of cell viability under stress conditions (i.e.  
561 hypoxia and nutrient deprivation) by induction of *KCNA5*. Our results suggest that  
562 KDM6B KO, independent of its demethylase activity, induces a sufficient level of stress  
563 to EwS cells, as shown by the increase in  $\gamma$ H2AX, to activate apoptosis upon EZH2  
564 inhibition. These results are in agreement with the specific induction of DNA repair  
565 pathways observed in KDM6B-depleted EwS cells. Besides, the non-specific  
566 demethylase inhibitor JIB-04 induces DNA damage in EwS cells (87). Future  
567 experiments should address the differential contribution of each demethylase to DNA  
568 damage and EZH2 functionality.

## 569 **Materials and methods**

### 570 **Mesenchymal stem cells and cell lines**

571 hpMSC were extracted from the healthy bone marrow of pediatric donors from HSJD and  
572 characterized according to described protocols (9, 88, 89). Cells were cultured at low  
573 confluence with Iscove's Modified Dulbecco's Medium (Gibco) supplemented with 10%



574 fetal newborn calf serum, 1% penicillin/streptomycin and 10 ng/mL of PDGF-BB  
575 (PeproTech).

576 The EwS cell lines, A673 and TC71, were purchased from ATCC. **Hela cells stably**  
577 **infected with doxycycline-inducible EWSR1-FLI1-3xFlag were kindly provided by Dr.**  
578 **de Álava and were induced as previously described (49).** They were cultured in RPMI  
579 1640 media (Gibco) and supplemented with 10% FBS, L-glutamine and  
580 penicillin/streptomycin. Cells were maintained in a humidified chamber at 37°C and 5%  
581 CO<sub>2</sub>, and split every 2-3 days when reaching confluence. EwS cells were treated with the  
582 EZH2 inhibitor GSK126 and the demethylase inhibitor GSKJ4 (both from Selleckchem)  
583 at 15 µM and 2.5 µM for 24 or 72 hours, respectively. DMSO was used as vehicle control.

#### 584 **Patient samples**

585 **This study was approved by the Institutional Review Boards. Written informed consent**  
586 **was obtained from patients or their legal guardians before collection of samples.** Biopsies  
587 from 45 primary EwS tumors at diagnosis from the HSJD Biobank, integrated in the  
588 Spanish Biobank Network of ISCIII and in the Xarxa de Tumors de Catalunya, were used  
589 for experimental purposes in agreement with the ethical committee procedures. Two  
590 samples were not appraisable for technical reasons and were excluded.

#### 591 **Lentiviral and transient transfections**

592 Infection was performed as previously described (20). Infected cells were selected with  
593 0.5-1 µg/mL puromycin for 72 hours and maintained in the first passages. Induction of  
594 the shRNA was performed with doxycycline hyclate (Sigma Aldrich) at 2 µg/mL for 72  
595 hours. Validation of the overexpression or knockdown was determined by Western blot.  
596 Target sequences for the SMARTvector inducible Tet-On shRNA system (Dharmacon)  
597 targeting KDM6A or KDM6B are described in table S7. Lentiviral plasmids pLV[Exp]-

598 Puro-EF1A for overexpressing KDM6A wild-type or a dead mutant enzyme with  
599 H1146A and E1148A mutations (53) were constructed and packaged by VectorBuilder  
600 and are described in table S7. **pInducer-JMJD3 WT and pInducer-JMJD3 HE > AA**  
601 **(H1390A/E1392A) were kindly gifted by Dr. Martínez-Balbás and were induced as**  
602 **previously described (81).** Empty and EWSR1-FLI1-pLIV vector was kindly provided by  
603 Dr. Rivera and published in Boulay *et al.* (18).

#### 604 **CRISPR/Cas9 genome editing**

605 KDM6A and KDM6B knockout cells were generated using the Gene Knockout Kit v2  
606 (Synthego) containing a pool of three validated sgRNA and exogenous Cas9 following  
607 manufacturers guidelines. CRISPR-edited cell pools were isolated by limit dilution in 96-  
608 well plates. Isolated clones were expanded and cells were collected for subsequent  
609 validation by Sanger sequencing of the PCR product. The Inference of CRISPR Edits  
610 (ICE) analysis software (90) was used to analyze the obtained sequences of edited cells  
611 (clones with a model fit  $R^2 > 0.6$  were only considered). Knockout clones were further  
612 validated by Western blot. Target sequences for the pool of three commercially  
613 predesigned sgRNA targeting KDM6A or KDM6B (Synthego) are described in table S7.

#### 614 **Cell viability, clonogenic assays and Annexin V staining**

615 Cell viability was determined by seeding EwS cell lines at  $0.25 \cdot 10^5$  cells/mL in clear  
616 bottom black walled 96-well Tissue Culture plates (Thermofisher) and incubated with 10  
617  $\mu$ L of Cell Titer Blue (Promega). Fluorescence was measured using the Infinite M Nano+  
618 (Tecan) microplate reader at  $560_{Ex}/590_{Em}$  nm. Clonogenic assays were performed by  
619 seeding  $0.12 \cdot 10^4$  cells/mL in 6-well plates and changing media every 2-3 days until  
620 visible colonies were grown in wells. Cells were then fixed for 10 minutes with 4%  
621 paraformaldehyd (Santa Cruz Biotech), washed with PBS and then incubated with a

622 crystal violet solution (2% W/V, 20% methanol in PBS) for 5 minutes. Quantification of  
623 the colony number was performed with the Image J (91) plugin ColonyArea  
624 (92). Cultured cells treated with the inhibitor were collected with trypsin, counted and re-  
625 suspended in Annexin binding buffer from the Alexa Fluor® 488 Annexin V/Dead Cell  
626 Apoptosis Kit (Thermofisher) following manufacturer's instructions. AnnexinV-stained  
627 cells were immediately run in Cytex Aurora CS full spectrum flow cytometer (Cytex  
628 Biosciences). FlowJo software version 10.2 was used to analyze collected data.

### 629 **RNA Extraction and Real-Time Quantitative RTqPCR**

630 Total RNA was isolated and purified using the RNeasy Mini Kit (Qiagen) following  
631 manufacturer's instructions. Quantification of RNA samples was performed using  
632 Nanodrop 1000 spectrophotometer (Thermo Fisher Scientific). Reverse transcription  
633 (RT) was performed using 1 µg of purified RNA and converted to cDNA with the  
634 retrotranscriptase M-MLV Reverse Transcriptase, the RNasin Plus RNase inhibitor and  
635 random primers (all from Promega). SYBR Green PCR Master Mix (Applied  
636 Biosystems) was used to perform quantitative PCR (qPCR) with QuantStudio 6 Flex  
637 (Applied Biosystems) using specific primer sequences (see table S7). Obtained data was  
638 normalized to housekeeping gene and analyzed with the  $2^{-\Delta\Delta CT}$  method relative to the  
639 experimental control condition. Data was performed in at least three independent  
640 biological experiments and expressed as mean  $\pm$ SEM.

### 641 **RNA-seq and Functional Analysis**

642 RNA-seq libraries were prepared with 0,5-1 µg of total high quality RNA collected from  
643 samples and the Illumina Stranded Total RNA Prep kit (Illumina) according to  
644 manufacturer's instructions. Fastq files were analyzed using FastQC software (93) to  
645 assess read quality. Adapters were removed and reads were trimmed using Cutadapt

646 software (94) according to per base Phred quality scores and minimum length. Reads  
647 were pseudoaligned to GRCh37 using Kallisto (95). Gene read counts from Kallisto were  
648 used to determine differential gene expression using R packages tximport (96) and  
649 DESeq2 (97). ERCC spike-ins were used for sample normalization and batch effect was  
650 removed using Limma package (98). Heatmaps were performed with heatmap2 R  
651 package. Gene set enrichment analysis (GSEA) was used to determine biologically  
652 relevant transcriptional events in gene sets from Hallmark Collection running each list  
653 with the KDM6A/KDM6B KO gene expression phenotype (99). Reports of functional  
654 enrichments of GO and other genomic libraries were generated using the EnrichR tool  
655 (100). Additional RNA data was obtained from A673 shFLI1 (GSE61953), the GEO  
656 repositories including 184 EwS tumors at diagnosis (GSE17679, GSE34620 and  
657 GSE37371), and from the Cancer cell line Encyclopedia (45).

## 658 **Immunohistochemistry**

659 Immunohistochemical analyses were performed following standard protocols. Fixed  
660 tumor xenografts were embedded in paraffin and cut in consecutive 2  $\mu$ m thick sections.  
661 Sections of paraffin tumors were deparaffinized, rehydrated in an alcohol battery and  
662 incubated with antigen retrieval with Epitope retrieval solution pH 6.0 (Novocastra  
663 Laboratories). Blocking with endogenous peroxidase was performed with Protein Block  
664 (Novocastra Laboratories) for 5 min and subsequent steps were performed in DAKO  
665 autostainer link 48 (Agilent Technologies, Inc.). Slides were counterstained in  
666 hematoxylin-eosin, dehydrated with alcohol and xylene and finally cover slipped with  
667 DPX. Nanozoomer 2.0 (Hamamatsu Photonics) was used to scan selected tumors for  
668 digital image processing. For KDM6A and KDM6B stains in EwS tumors  
669 immunohistochemical semi-quantification was scored by an independent pathologist. A  
670 semiquantitative histoscore (H-score) value was calculated based on a linear combination

671 of the intensity and proportion of stained cells per camp that punctuates strongly stained  
672 nuclei (SSN), the percentage of moderately stained nuclei (MSN), and the percentage of  
673 weakly stained nuclei (WSN) following the following formula:  $H\text{-score} = 1 \times WSN + 2$   
674  $\times MSN + 3 \times SSN$ . The H-score value ranges possible scores from 0 to 300 (101). For  
675 tumor xenografts H-score was calculated with IHC-Profiler (102) and ImageJ software  
676 based on staining intensity and percentage of positive staining cells, and high positive  
677 staining scored 3, positive staining scored 2, low positive scored staining 1, and negative  
678 staining scored 0. The list of primary antibodies and dilutions used are listed in table S7.

### 679 **Protein Extract Preparation, immunoprecipitation and Western blotting**

680 Whole cell protein extracts were prepared in RIPA buffer (10 mM Tris-HCl pH 8, 1 mM  
681 EDTA, 0.5 mM EGTA, 1% Triton X-100, 0.1% sodium deoxycolate, 0.1% SDS, and 140  
682 mM NaCl) containing phosphatase and EDTA-free Protease Inhibitor Cocktail (Roche).  
683 Cell lysates incubated on ice for 30 min were centrifuged at 12,000 rpm for 15 min at  
684 4°C. Histone extracts were isolated using the EpiQuick Histone Extraction kit (Epigentek)  
685 following manufacturer's instructions. Protein supernatants were collected and quantified  
686 by Bradford assay (Sigma Aldrich). **Immunoprecipitation was performed with total**  
687 **cellular extracts incubated at 4°C overnight with primary antibody followed by incubation**  
688 **with Dynabeads Protein A (Invitrogen). Immunoprecipitated samples, 50 µg of whole**  
689 **cell extract or 5 µg of histone protein extracts were mixed with loading Laemmli buffer**  
690 **with DTT for Western blot experiments following standard protocols. The primary**  
691 **antibodies and dilutions are listed (see table S7) and secondary antibodies goat anti-rabbit**  
692 **and goat anti-mouse IRDye (Li-COR Biosciences) were diluted 1:10,000 an incubated**  
693 **for 1 h at room temperature to blotted membranes. Nitrocellulose membranes (Amershan**  
694 **Protran) were scanned and visualized with Li-COR Odyssey Infrared Imaging System**  
695 **(Li-COR Biosciences).**

## 696 **ChIP-qPCR**

697 ChIP-qPCR assays were performed as previously described (103). Cultured cells were  
698 fixed using 1% of methanol-free formaldehyde (Thermo Fisher Scientific) for 10 min at  
699 room temperature, and crosslinking was stopped by adding 500  $\mu$ L of glycine (1.25 M).  
700 Lysis was performed in soft lysis buffer (0.1% SDS, 0.15 M NaCl, 1% Triton X-100, 1  
701 mM EDTA, and 20 mM Tris pH 8) supplemented with 1 mg/mL of protease inhibitors  
702 (Roche). Cell lysates were sonicated for 10 cycles with Bioruptor Pico (Diagenode) until  
703 chromatin was sheared to an average length of 200 bp. After centrifugation, a small  
704 fraction of eluted chromatin was measured with Qubit dsDNA HS kit (ThermoFisher  
705 Scientific). Immunoprecipitations were prepared starting with 30  $\mu$ g for each antibody  
706 and incubated overnight at 4°C in a rotating wheel (see table S7). 50  $\mu$ L of Dynabeads  
707 Protein A (Invitrogen) were added to samples, and the slurry was incubated for 2 hours  
708 to capture DNA fragments. Immunoprecipitates were washed with the following buffers:  
709 TSE I (0.1% SDS, 1% Triton X-100, 2 mM EDTA, 20 mM Tris-HCl pH 8, 150 mM  
710 NaCl), TSE II (0.1% SDS, 1% Triton X-100, 2 mM EDTA, 20 mM Tris-HCl pH 8, 500  
711 mM NaCl), TSEIII (0.25 M LiCl, 1% Nonidet P-40, 1% deoxycholate, 1 mM EDTA, 10  
712 mM Tris-HCl pH 8), and Tris-EDTA buffer. All incubation and washing steps were  
713 performed in a rotating wheel at 4°C to avoid protein degradation. DNA captured by the  
714 beads was eluted by adding 120  $\mu$ L of a solution containing 1% SDS, 0.1 M NaHCO<sub>3</sub>  
715 and decrosslinked at 65°C for 3 hours with gentle shaking. Genomic DNA fragments from  
716 ChIP samples were purified with QIAquick PCR Purification kit (Qiagen) and eluted in  
717 50-100  $\mu$ L of Tris-EDTA buffer. Differences in DNA content from ChIP assays were  
718 determined by qPCR using the SQ6 Real Time PCR System and SYBR Green master mix  
719 (Applied Biosystems). The reported data from at least three independent experiments

720 represent real-time PCR values normalized to input DNA and are expressed as percentage  
721 of bound/input signal and presented as mean±SEM.

## 722 **ChIP-seq and Bioinformatic Analysis**

723 ChIP-seq libraries were prepared using 2-5 ng of input and ChIP samples and the kit  
724 NEBNext Ultra DNA Library Prep for Illumina (New England Biolabs) following  
725 manufacturer's protocol. All purification steps were performed using Agen Court  
726 AMPure XP beads (Qiagen). NEBNext Multiplex oligonucleotides for Illumina (New  
727 England Biolabs) was used for library amplification. Quality control and fragment size  
728 was analyzed using Agilent High Sensitivity ChIP and quantified with KAPA Library  
729 Quantification Kit (KapaBiosystems). ChIP-seq data from DNA and input samples were  
730 sequenced with Hiseq 2500 Illumina sequencing system.

731 ChIP-seq samples were mapped against the hg19 human genome assembly using Bowtie  
732 with the option -m 1 to discard those reads that could not be uniquely mapped to just one  
733 region (104). ChIP-seq samples normalized by spike-in were mapped against a synthetic  
734 genome constituted by the human and the fruit fly chromosomes (hg19 + dm3) using  
735 Bowtie with the option -m 1 to discard reads that did not map uniquely to one region.  
736 MACS was run with the default parameters but with the shift-size adjusted to 100 bp to  
737 perform the peak calling against the corresponding control sample (105). DiffBind (106)  
738 was run next over the union of peaks from each pair of replicates of the same experiment  
739 to find the peaks significantly enriched in both replicates in comparison to the  
740 corresponding controls (DiffBind 2.0 arguments: categories = DBA\_CONDITION, block  
741 = DBA\_REPLICATE and method = DBA\_DESEQ2\_BLOCK).

742 We used SeqCode (107) for ChIP-seq downstream analysis across multiple stages: (i) the  
743 genome distribution of each set of peaks was generated by counting the number of peaks

744 fitted on each class of region according to RefSeq annotations (*108*). Promoter is the  
745 region between 2.5 kb upstream and 2.5 kb downstream of the transcription start site  
746 (TSS). Genic regions correspond to the rest of the gene (the part that is not classified as  
747 promoter) and the rest of the genome is considered to be intergenic. Peaks that overlapped  
748 with more than one genomic feature were proportionally counted the same number of  
749 times; (ii) aggregated plots showing the average distribution of ChIP-seq reads around  
750 the TSS or along the gene body of each target gene were generated by counting the  
751 number of reads for each region according to RefSeq and then averaging the values for  
752 the total number of mapped reads of each sample and the total number of genes in the  
753 particular gene set; (iii) heatmaps displaying ChIP-seq signal strength around the summit  
754 of each peak were generated by counting the number of reads in this region for each  
755 individual peak and normalizing this value with the total number of mapped reads of the  
756 sample. Peaks on each heatmap were ranked by the logarithm of the average number of  
757 reads in the same genomic region; (iv) boxplots showing the ChIP-seq level distribution  
758 for a particular ChIP experiment on a set of genomic peaks were calculated by  
759 determining the maximum value on this region at this sample, which was assigned  
760 afterwards to the corresponding peak. To quantify genome-wide differences on  
761 H3K27me3 gain/loss, we performed a similar approach over the full set of bins of 1 kb  
762 (average value per bin, genome assembly: hg19) ; (v) BedGraph profiles were generated  
763 from each set of mapped reads and uploaded into the UCSC genome browser to generate  
764 the screenshots of tracks along the manuscript (*109*); (vi) the set of target genes of a  
765 biological feature was found by matching all ChIP-seq peaks in the region 2.5 kb  
766 upstream of the TSS until the end of the transcripts as annotated in RefSeq.

767 To build our collection of enhancers and promoters, we reanalyzed published ChIP-seq  
768 samples of H3K4me1, H3K27ac, H3K27me3, and H3K4me3 in A673 cells (*16*). Each



769 class of enhancer and promoter categories were defined as in Blanco *et al.* (46). Promoters  
770 were defined as ChIP peaks of H3K27 found up to 2.5 kb from the TSS of one gene and  
771 enhancers on intergenic areas outside promoters or within gene introns. H3K4me3 was  
772 required to be present in promoters but absent in enhancers. We defined five classes of  
773 regulatory elements: active enhancers (H3K27ac), active promoters (H3K27ac +  
774 H3K4me3), poised enhancers (H3K27me3), primed enhancers (H3K4me1 without  
775 H3K27ac) and bivalent promoters (H3K27me3 + H3K4me3). To construct the list of  
776 putative targets of KDM6A/KDM6B enhancers, we identified the list of genes in the  
777 vicinity of overlapping KDM6A+EWSR1-FLI1 and KDM6B+EWSR1-FLI1 modules  
778 (maximum distance between peaks and differentially regulated genes: 100 kb). Reports  
779 of functional enrichments of GO and other genomic libraries were generated using the  
780 EnrichR tool (100). Motif analysis of the sequences of ChIP-seq peaks was performed  
781 with the MEME-ChIP tool, adjusting the MEME motif width between 5 and 15 bps (110).  
782 ChIP-seq raw data from H3K27me3 in control and EWSR1-FLI1 hpMSC was kindly  
783 provided by Dr Nicolo Riggi and Dr Miguel Rivera (accession number GSE106925). For  
784 ChIP-seq experiments with EWSR1-FLI1 in EWS cell lines we used an antibody that  
785 correlates 62% at peak level with published data (16) and nicely reproduce our previous  
786 data with RING1B overlap (20) (see table S7).

### 787 **Murine xenograft studies**

788 *In vivo* studies were performed after the approval of the Institutional Animal Research  
789 Ethics Committee and by the animal experimentation commission of the Catalan  
790 government.  $1 \cdot 10^6$  cells of parental, KDM6 knockout (sgRNA#1 and 2) and non-targeting  
791 control (sgCTRL) A673 or TC71 cells in 200  $\mu$ L of PBS with Matrigel (Becton  
792 Dickinson) were subcutaneously injected in two flanks of Athymic Nude mice (Envigo)  
793 (for A673 cells: n=11 for parental, n=11 sgKDM6A#1, n=9 sgCTRL; n=9 for parental,

794 n=7 sgKDM6A#2 and n=12 sgCTRL; n=8 for sgCTRL and n=11 sgKDM6B#1 and #2;  
795 for TC71 cells: n=10 for sgCTRL, n= 9 sgKDM6A#1 and n= 9 sgKDM6A#2, n indicates  
796 number of tumors). Tumor growth was monitored three times per week by measuring  
797 growing tumors with a digital caliper. Mice were sacrificed when tumors reached a  
798 volume of 1500mm<sup>3</sup> and tumors were excised. Collected tumors were divided in parts:  
799 one part was frozen for protein experiments and the other was fixed in 10% formalin for  
800 immunohistochemistry experiments. For RNA experiments 4 tumors of each  
801 experimental group were dissociated with collagenase IV (50 mg/mL) (Sigma) and a  
802 tissue chopper (Ted Pella, Inc). Then tissue homogenates were digested with 5 mg/mL of  
803 DNase I (Sigma) and trypsin/EDTA (0.25%) to subsequently separate mouse stroma  
804 cells from human cells with Mouse Cell Depletion kit (Milteny Biotech) following  
805 manufacturer's guidelines. Log-rank test was used to calculate significance of the groups  
806 in Kaplan-Meier.

### 807 **Quantification and statistical analyses**

808 Data was analyzed using Graphpad Prism 9 software (San Diego, CA, USA) version  
809 v.9.1.2 and expressed as mean ±SEM or SD as indicated in figure legends. Kruskal-Wallis  
810 one-way analysis of variance (ANOVA) and two-way ANOVA with Tukey's correction  
811 (for non-normally distributed data) were applied to determine differences between  
812 multiple groups. Holm-Šídák or Dunn's tests were used for multiple comparison tests.  
813 Student t-test and Mann-Whitney t-test (for non-normally distributed data) were used for  
814 non-paired comparisons of two groups. Kaplan-Meier curves were compared with the  
815 log-rank (Mantel-Cox) test. Statistically significant differences among groups are  
816 annotated in each graph of the manuscript and the statistical tests applied can be found in  
817 the figure legends. \*P<0.05, \*\*P<0.01, \*\*\*P<0.001, P\*\*\*\*<0.0001.

818 **References**

- 819 1. T. G. P. Grünewald, F. Cidre-Aranaz, D. Surdez, E. M. Tomazou, E. de Álava, H.  
820 Kovar, P. H. Sorensen, O. Delattre, U. Dirksen, Ewing sarcoma. *Nat. Rev. Dis.*  
821 *Primers* **4**, 5 (2018).
- 822 2. A. S. Brohl, D. A. Solomon, W. Chang, J. Wang, Y. Song, S. Sindiri, R. Patidar,  
823 L. Hurd, L. Chen, J. F. Shern, H. Liao, X. Wen, J. Gerard, J. S. Kim, J. A. Lopez  
824 Guerrero, I. Machado, D. H. Wai, P. Picci, T. Triche, A. E. Horvai, M. Miettinen,  
825 J. S. Wei, D. Catchpool, A. Llombart-Bosch, T. Waldman, J. Khan, The genomic  
826 landscape of the Ewing Sarcoma family of tumors reveals recurrent STAG2  
827 mutation. *PLoS Genet.* **10**, e1004475 (2014).
- 828 3. B. D. Crompton, C. Stewart, A. Taylor-Weiner, G. Alexe, K. C. Kurek, M. L.  
829 Calicchio, A. Kiezun, S. L. Carter, S. A. Shukla, S. S. Mehta, A. R. Thorner, C.  
830 de Torres, C. Lavarino, M. Suñol, A. McKenna, A. Sivachenko, K. Cibulskis, M.  
831 S. Lawrence, P. Stojanov, M. Rosenberg, L. Ambrogio, D. Auclair, S. Seepo, B.  
832 Blumenstiel, M. DeFelice, I. Imaz-Rosshandler, A. Schwarz-Cruz y Celis, M. N.  
833 Rivera, C. Rodriguez-Galindo, M. D. Fleming, T. R. Golub, G. Getz, J. Mora, K.  
834 Stegmaier, The Genomic Landscape of Pediatric Ewing Sarcoma. *Cancer Discov.*  
835 **4**, 1326-1341 (2014).
- 836 4. S. Behjati, R. J. Gilbertson, S. M. Pfister, Maturation Block in Childhood Cancer.  
837 *Cancer Discov.* **11**, 542-544 (2021).
- 838 5. O. Delattre, J. Zucman, B. Plougastel, C. Desmaze, T. Melot, M. Peter, H. Kovar,  
839 I. Joubert, P. de Jong, G. Rouleau, A. Aurias, G. Thomas, Gene fusion with an  
840 ETS DNA-binding domain caused by chromosome translocation in human  
841 tumours. *Nature* **359**, 162-165 (1992).
- 842 6. S. L. Lessnick, B. S. Braun, C. T. Denny, W. A. May, Multiple domains mediate  
843 transformation by the Ewing's sarcoma EWS/FLI-1 fusion gene. *Oncogene* **10**,  
844 423-431 (1995).
- 845 7. W. A. May, M. L. Gishizky, S. L. Lessnick, L. B. Lunsford, B. C. Lewis, O.  
846 Delattre, J. Zucman, G. Thomas, C. T. Denny, Ewing sarcoma 11;22 translocation  
847 produces a chimeric transcription factor that requires the DNA-binding domain  
848 encoded by FLI1 for transformation. *Proc. Natl. Acad. Sci. U.S.A* **90**, 5752-5756  
849 (1993).
- 850 8. M. Patel, J. M. Simon, M. D. Iglesia, S. B. Wu, A. W. McFadden, J. D. Lieb, I. J.  
851 Davis, Tumor-specific retargeting of an oncogenic transcription factor chimera  
852 results in dysregulation of chromatin and transcription. *Genome Res.* **22**, 259-270  
853 (2012).
- 854 9. N. Riggi, M. L. Suvà, D. Suvà, L. Cironi, P. Provero, S. Tercier, J. M. Joseph, J.  
855 C. Stehle, K. Baumer, V. Kindler, I. Stamenkovic, EWS-FLI-1 Expression  
856 Triggers a Ewing's Sarcoma Initiation Program in Primary Human Mesenchymal  
857 Stem Cells. *Cancer Res.* **68**, 2176-2185 (2008).
- 858 10. C. von Levetzow, X. Jiang, Y. Gwyne, G. von Levetzow, L. Hung, A. Cooper, J.  
859 H. Hsu, E. R. Lawlor, Modeling initiation of Ewing sarcoma in human neural crest  
860 cells. *PloS one* **6**, e19305 (2011).
- 861 11. B. Deneen, C. T. Denny, Loss of p16 pathways stabilizes EWS/FLI1 expression  
862 and complements EWS/FLI1 mediated transformation. *Oncogene* **20**, 6731-6741  
863 (2001).
- 864 12. S. L. Lessnick, C. S. Dacwag, T. R. Golub, The Ewing's sarcoma oncoprotein  
865 EWS/FLI induces a p53-dependent growth arrest in primary human fibroblasts.  
866 *Cancer Cell* **1**, 393-401 (2002).

- 867 13. N. Riggi, M. L. Suvà, C. De Vito, P. Provero, J. C. Stehle, K. Baumer, L. Cironi,  
868 M. Janiszewska, T. Petricevic, D. Suvà, S. Tercier, J. M. Joseph, L. Guillou, I.  
869 Stamenkovic, EWS-FLI-1 modulates miRNA145 and SOX2 expression to initiate  
870 mesenchymal stem cell reprogramming toward Ewing sarcoma cancer stem cells.  
871 *Genes Dev.* **24**, 916-932 (2010).
- 872 14. K. Gangwal, D. Close, C. A. Enriquez, C. P. Hill, S. L. Lessnick, Emergent  
873 Properties of EWS/FLI Regulation via GGAA Microsatellites in Ewing's  
874 Sarcoma. *Genes Cancer* **1**, 177-187 (2010).
- 875 15. K. Gangwal, S. Sankar, P. C. Hollenhorst, M. Kinsey, S. C. Haroldsen, A. A.  
876 Shah, K. M. Boucher, W. S. Watkins, L. B. Jorde, B. J. Graves, S. L. Lessnick,  
877 Microsatellites as EWS/FLI response elements in Ewing's sarcoma. *Proc. Natl.*  
878 *Acad. Sci. U.S.A* **105**, 10149-10154 (2008).
- 879 16. N. Riggi, B. Knoechel, S. M. Gillespie, E. Rheinbay, G. Boulay, M. L. Suvà, N.  
880 E. Rossetti, W. E. Boonseng, O. Oksuz, E. B. Cook, A. Formey, A. Patel, M.  
881 Gymrek, V. Thapar, V. Deshpande, D. T. Ting, F. J. Hornicek, G. P. Nielsen, I.  
882 Stamenkovic, M. J. Aryee, B. E. Bernstein, M. N. Rivera, EWS-FLI1 utilizes  
883 divergent chromatin remodeling mechanisms to directly activate or repress  
884 enhancer elements in Ewing sarcoma. *Cancer Cell* **26**, 668-681 (2014).
- 885 17. E. M. Tomazou, N. C. Sheffield, C. Schmidl, M. Schuster, A. Schönegger, P.  
886 Datlinger, S. Kubicek, C. Bock, H. Kovar, Epigenome mapping reveals distinct  
887 modes of gene regulation and widespread enhancer reprogramming by the  
888 oncogenic fusion protein EWS-FLI1. *Cell Rep* **10**, 1082-1095 (2015).
- 889 18. G. Boulay, G. J. Sandoval, N. Riggi, S. Iyer, R. Buisson, B. Naigles, M. E. Awad,  
890 S. Rengarajan, A. Volorio, M. J. McBride, L. C. Broye, L. Zou, I. Stamenkovic,  
891 C. Kadoch, M. N. Rivera, Cancer-Specific Retargeting of BAF Complexes by a  
892 Prion-like Domain. *Cell* **171**, 163-178. (2017).
- 893 19. B. Schuettengruber, H.-M. Bourbon, L. Di Croce, G. Cavalli, Genome Regulation  
894 by Polycomb and Trithorax: 70 Years and Counting. *Cell* **171**, 34-57 (2017).
- 895 20. S. Sánchez-Molina, E. Figuerola-Bou, E. Blanco, M. Sánchez-Jiménez, P.  
896 Táboas, S. Gómez, C. Ballaré, D. J. García-Domínguez, E. Prada, L. Hontecillas-  
897 Prieto, Á. M. Carcaboso, Ó. M. Tirado, I. Hernández-Muñoz, E. de Álava, C.  
898 Lavarino, L. Di Croce, J. Mora, RING1B recruits EWSR1-FLI1 and cooperates  
899 in the remodeling of chromatin necessary for Ewing sarcoma tumorigenesis. *Sci.*  
900 *Adv.* **6**, eaba3058 (2020).
- 901 21. L. A. Owen, A. A. Kowalewski, S. L. Lessnick, EWS/FLI mediates transcriptional  
902 repression via NKX2.2 during oncogenic transformation in Ewing's sarcoma.  
903 *PloS one* **3**, e1965 (2008).
- 904 22. T. Ezponda, J. D. Licht, Molecular Pathways: Deregulation of Histone H3 Lysine  
905 27 Methylation in Cancer—Different Paths, Same Destination. *Clin. Cancer. Res.*  
906 **20**, 5001-5008 (2014).
- 907 23. R. Margueron, D. Reinberg, The Polycomb complex PRC2 and its mark in life.  
908 *Nature* **469**, 343-349 (2011).
- 909 24. I. Comet, E. M. Riising, B. Leblanc, K. Helin, Maintaining cell identity: PRC2-  
910 mediated regulation of transcription and cancer. *Nat. Rev. Cancer* **16**, 803-810  
911 (2016).
- 912 25. P. Chammas, I. Mocavini, L. Di Croce, Engaging chromatin: PRC2 structure  
913 meets function. *Br. J. Cancer* **122**, 315-328 (2020).
- 914 26. K. Agger, P. A. C. Cloos, J. Christensen, D. Pasini, S. Rose, J. Rappsilber, I.  
915 Issaeva, E. Canaani, A. E. Salcini, K. Helin, UTX and JMJD3 are histone H3K27

- 916 demethylases involved in HOX gene regulation and development. *Nature* **449**,  
917 731-734 (2007).
- 918 27. M. G. Lee, J. Norman, A. Shilatifard, R. Shiekhatar, Physical and Functional  
919 Association of a Trimethyl H3K4 Demethylase and Ring6a/MBLR, a Polycomb-  
920 like Protein. *Cell* **128**, 877-887 (2007).
- 921 28. Y. Shan, Y. Zhang, Y. Zhao, T. Wang, J. Zhang, J. Yao, N. Ma, Z. Liang, W.  
922 Huang, K. Huang, T. Zhang, Z. Su, Q. Chen, Y. Zhu, C. Wu, T. Zhou, W. Sun, Y.  
923 Wei, C. Zhang, C. Li, S. Su, B. Liao, M. Zhong, X. Zhong, J. Nie, D. Pei, G. Pan,  
924 JMJD3 and UTX determine fidelity and lineage specification of human neural  
925 progenitor cells. *Nat. Commun.* **11**, 382 (2020).
- 926 29. S. Lee, J. W. Lee, S. K. Lee, UTX, a histone H3-lysine 27 demethylase, acts as a  
927 critical switch to activate the cardiac developmental program. *Dev. Cell* **22**, 25-37  
928 (2012).
- 929 30. S. P. Wang, Z. Tang, C. W. Chen, M. Shimada, R. P. Koche, L. H. Wang, T.  
930 Nakadai, A. Chramiec, A. V. Krivtsov, S. A. Armstrong, R. G. Roeder, A UTX-  
931 MLL4-p300 Transcriptional Regulatory Network Coordinately Shapes Active  
932 Enhancer Landscapes for Eliciting Transcription. *Mol. Cell* **67**, 308-321. (2017).
- 933 31. R. Fueyo, S. Iacobucci, S. Pappa, C. Estarás, S. Lois, M. Vicioso-Mantis, C.  
934 Navarro, S. Cruz-Molina, J. C. Reyes, Á. Rada-Iglesias, X. de la Cruz, M. A.  
935 Martínez-Balbás, Lineage specific transcription factors and epigenetic regulators  
936 mediate TGFβ-dependent enhancer activation. *Nucleic Acids Res.* **46**, 3351-3365  
937 (2018).
- 938 32. Y. Huang, H. Zhang, L. Wang, C. Tang, X. Qin, X. Wu, M. Pan, Y. Tang, Z.  
939 Yang, I. A. Babarinde, R. Lin, G. Ji, Y. Lai, X. Xu, J. Su, X. Wen, T. Satoh, T.  
940 Ahmed, V. Malik, C. Ward, G. Volpe, L. Guo, J. Chen, L. Sun, Y. Li, X. Huang,  
941 X. Bao, F. Gao, B. Liu, H. Zheng, R. Jauch, L. Lai, G. Pan, J. Chen, G. Testa, S.  
942 Akira, J. Hu, D. Pei, A. P. Hutchins, M. A. Esteban, B. Qin, JMJD3 acts in tandem  
943 with KLF4 to facilitate reprogramming to pluripotency. *Nat. Commun.* **11**, 5061  
944 (2020).
- 945 33. P. Das, J. H. Taube, Regulating Methylation at H3K27: A Trick or Treat for  
946 Cancer Cell Plasticity. *Cancers (Basel)* **12**, (2020).
- 947 34. K. H. Kim, C. W. Roberts, Targeting EZH2 in cancer. *Nat. Med.* **22**, 128-134  
948 (2016).
- 949 35. K. M. Arcipowski, C. A. Martinez, P. Ntziachristos, Histone demethylases in  
950 physiology and cancer: a tale of two enzymes, JMJD3 and UTX. *Curr. Opin.*  
951 *Genet. Dev.* **36**, 59-67 (2016).
- 952 36. A. Benyoucef, C. G. Pali, C. Wang, C. J. Porter, A. Chu, F. Dai, V. Tremblay, P.  
953 Rakopoulos, K. Singh, S. Huang, F. Pflumio, J. Hébert, J. F. Couture, T. J.  
954 Perkins, K. Ge, F. J. Dilworth, M. Brand, UTX inhibition as selective epigenetic  
955 therapy against TAL1-driven T-cell acute lymphoblastic leukemia. *Genes Dev.*  
956 **30**, 508-521 (2016).
- 957 37. X. Leng, J. Wang, N. An, X. Wang, Y. Sun, Z. Chen, Histone 3 lysine-27  
958 demethylase KDM6A coordinates with KMT2B to play an oncogenic role in  
959 NSCLC by regulating H3K4me3. *Oncogene* **39**, 6468--6479 (2020).
- 960 38. P. Ntziachristos, A. Tsirigos, G. G. Welstead, T. Trimarchi, S. Bakogianni, L. Xu,  
961 E. Loizou, L. Holmfeldt, A. Strikoudis, B. King, J. Mullenders, J. Becksfort, J.  
962 Nedjic, E. Paietta, M. S. Tallman, J. M. Rowe, G. Tonon, T. Satoh, L. Kruidenier,  
963 R. Prinjha, S. Akira, P. Van Vlierberghe, A. A. Ferrando, R. Jaenisch, C. G.  
964 Mullighan, I. Aifantis, Contrasting roles of histone 3 lysine 27 demethylases in  
965 acute lymphoblastic leukaemia. *Nature* **514**, 513-517 (2014).

- 966 39. J. van der Meulen, V. Sanghvi, K. Mavrakis, K. Durinck, F. Fang, F. Matthijssens,  
967 P. Rondou, M. Rosen, T. Pieters, P. Vandenberghe, E. Delabesse, T. Lammens,  
968 B. De Moerloose, B. Menten, N. Van Roy, B. Verhasselt, B. Poppe, Y. Benoit, T.  
969 Taghon, A. M. Melnick, F. Speleman, H. G. Wendel, P. Van Vlierberghe, The  
970 H3K27me3 demethylase UTX is a gender-specific tumor suppressor in T-cell  
971 acute lymphoblastic leukemia. *Blood* **125**, 13-21 (2015).
- 972 40. G. Boulay, A. Volorio, S. Iyer, L. C. Broye, I. Stamenkovic, N. Riggi, M. N.  
973 Rivera, Epigenome editing of microsatellite repeats defines tumor-specific  
974 enhancer functions and dependencies. *Genes Dev.* **32**, 1008-1019 (2018).
- 975 41. G. H. Richter, S. Plehm, A. Fasan, S. Rössler, R. Unland, I. M. Bennani-Baiti, M.  
976 Hotfilder, D. Löwel, I. von Luettichau, I. Mossbrugger, L. Quintanilla-Martinez,  
977 H. Kovar, M. S. Staeger, C. Müller-Tidow, S. Burdach, EZH2 is a mediator of  
978 EWS/FLI1 driven tumor growth and metastasis blocking endothelial and neuro-  
979 ectodermal differentiation. *Proc. Natl. Acad. Sci. U.S.A* **106**, 5324-5329 (2009).
- 980 42. S. Bilke, R. Schwentner, F. Yang, M. Kauer, G. Jug, R. L. Walker, S. Davis, Y.  
981 J. Zhu, M. Pineda, P. S. Meltzer, H. Kovar, Oncogenic ETS fusions deregulate  
982 E2F3 target genes in Ewing sarcoma and prostate cancer. *Genome Res.* **23**, 1797-  
983 1809 (2013).
- 984 43. L. K. Svoboda, A. Harris, N. J. Bailey, R. Schwentner, E. Tomazou, C. von  
985 Levetzow, B. Magnuson, M. Ljungman, H. Kovar, E. R. Lawlor, Overexpression  
986 of HOX genes is prevalent in Ewing sarcoma and is associated with altered  
987 epigenetic regulation of developmental transcription programs. *Epigenetics* **9**,  
988 1613-1625 (2014).
- 989 44. K. B. Hahm, K. Cho, C. Lee, Y. H. Im, J. Chang, S. G. Choi, P. H. Sorensen, C.  
990 J. Thiele, S. J. Kim, Repression of the gene encoding the TGF-beta type II receptor  
991 is a major target of the EWS-FLI1 oncoprotein. *Nat. Genet.* **23**, 222-227 (1999).
- 992 45. J. Barretina, G. Caponigro, N. Stransky, K. Venkatesan, A. A. Margolin, S. Kim,  
993 C. J. Wilson, J. Lehár, G. V. Kryukov, D. Sonkin, A. Reddy, M. Liu, L. Murray,  
994 M. F. Berger, J. E. Monahan, P. Morais, J. Meltzer, A. Korejwa, J. Jané-Valbuena,  
995 F. A. Mapa, J. Thibault, E. Bric-Furlong, P. Raman, A. Shipway, I. H. Engels, J.  
996 Cheng, G. K. Yu, J. Yu, P. Aspesi, M. de Silva, K. Jagtap, M. D. Jones, L. Wang,  
997 C. Hatton, E. Palesscandolo, S. Gupta, S. Mahan, C. Sougnez, R. C. Onofrio, T.  
998 Liefeld, L. MacConaill, W. Winckler, M. Reich, N. Li, J. P. Mesirov, S. B.  
999 Gabriel, G. Getz, K. Ardlie, V. Chan, V. E. Myer, B. L. Weber, J. Porter, M.  
1000 Warmuth, P. Finan, J. L. Harris, M. Meyerson, T. R. Golub, M. P. Morrissey, W.  
1001 R. Sellers, R. Schlegel, L. A. Garraway, The Cancer Cell Line Encyclopedia  
1002 enables predictive modelling of anticancer drug sensitivity. *Nature* **483**, 603  
1003 (2012).
- 1004 46. E. Blanco, M. González-Ramírez, A. Alcaine-Colet, S. Aranda, L. Di Croce, The  
1005 Bivalent Genome: Characterization, Structure, and Regulation. *Trends Genet.* **36**,  
1006 118-131 (2020).
- 1007 47. J. Drouin, Minireview: Pioneer Transcription Factors in Cell Fate Specification.  
1008 *Mol. Endocrinol.* **28**, 989-998 (2014).
- 1009 48. S. S. Maurya, Role of Enhancers in Development and Diseases. *Epigenomes* **5**, 21  
1010 (2021).
- 1011 49. D. J. García-Domínguez, L. Hontecillas-Prieto, E. A. León, S. Sánchez-Molina,  
1012 P. Rodríguez-Núñez, F. J. Morón, N. Hajji, C. Mackintosh, E. de Álava, An  
1013 inducible ectopic expression system of EWSR1-FLI1 as a tool for understanding  
1014 Ewing sarcoma oncogenesis. *PloS one* **15**, e0234243 (2020).

- 1015 50. A. D'Oto, J. Fang, H. Jin, B. Xu, S. Singh, A. Mullasseril, V. Jones, A. Abu-Zaid,  
1016 X. von Buttlar, B. Cooke, D. Hu, J. Shohet, A. J. Murphy, A. M. Davidoff, J.  
1017 Yang, KDM6B promotes activation of the oncogenic CDK4/6-pRB-E2F pathway  
1018 by maintaining enhancer activity in MYCN-amplified neuroblastoma. *Nat.*  
1019 *Commun.* **12**, 7204 (2021).
- 1020 51. K. B. Shpargel, J. Starmer, C. Wang, K. Ge, T. Magnuson, UTX-guided neural  
1021 crest function underlies craniofacial features of Kabuki syndrome. *Proc. Natl.*  
1022 *Acad. Sci. U.S.A* **114**, E9046-E9055 (2017).
- 1023 52. C. Wang, J. E. Lee, Y. W. Cho, Y. Xiao, Q. Jin, C. Liu, K. Ge, UTX regulates  
1024 mesoderm differentiation of embryonic stem cells independent of H3K27  
1025 demethylase activity. *Proc. Natl. Acad. Sci. U.S.A* **109**, 15324-15329 (2012).
- 1026 53. A. A. Mansour, O. Gafni, L. Weinberger, A. Zviran, M. Ayyash, Y. Rais, V.  
1027 Krupalnik, M. Zerbib, D. Amann-Zalcenstein, I. Maza, S. Geula, S. Viukov, L.  
1028 Holtzman, A. Pribluda, E. Canaani, S. Horn-Saban, I. Amit, N. Novershtern, J. H.  
1029 Hanna, The H3K27 demethylase Utx regulates somatic and germ cell epigenetic  
1030 reprogramming. *Nature* **488**, 409-413 (2012).
- 1031 54. M. Gozdecka, E. Meduri, M. Mazan, K. Tzelepis, UTX-mediated enhancer and  
1032 chromatin remodeling suppresses myeloid leukemogenesis through noncatalytic  
1033 inverse regulation of ETS and GATA programs. *Nat Genet.* **50**, 883-894 (2018).
- 1034 55. S. A. Miller, S. E. Mohn, A. S. Weinmann, Jmjd3 and UTX play a demethylase-  
1035 independent role in chromatin remodeling to regulate T-box family member-  
1036 dependent gene expression. *Mol. Cell* **40**, 594-605 (2010).
- 1037 56. L. Seunghye, W. L. Jae , L. Soo-Kyung, UTX, a Histone H3-Lysine 27  
1038 Demethylase, Acts as a Critical Switch to Activate the Cardiac Developmental  
1039 Program. *Dev. Cell* **22**, 25-37 (2012).
- 1040 57. M. L. Phelan, S. Sif, G. J. Narlikar, R. E. Kingston, Reconstitution of a core  
1041 chromatin remodeling complex from SWI/SNF subunits. *Mol. Cell* **3**, 247-253  
1042 (1999).
- 1043 58. P. M. Steinert, D. R. Roop, Molecular and cellular biology of intermediate  
1044 filaments. *Annu. Rev. Biochem.* **57**, 593-625 (1988).
- 1045 59. M. Lipinski, K. Braham, I. Philip, J. Wiels, T. Philip, K. Dellagi, C. Goridis, G.  
1046 M. Lenoir, T. Tursz, Phenotypic characterization of Ewing sarcoma cell lines with  
1047 monoclonal antibodies. *J. Cell. Biochem.* **31**, 289-296 (1986).
- 1048 60. A. O. Cavazzana, J. S. Miser, J. Jefferson, T. J. Triche, Experimental evidence for  
1049 a neural origin of Ewing's sarcoma of bone. *Am J Pathol* **127**, 507-518 (1987).
- 1050 61. R. Moll, I. Lee, V. E. Gould, R. Berndt, A. Roessner, W. W. Franke,  
1051 Immunocytochemical analysis of Ewing's tumors. Patterns of expression of  
1052 intermediate filaments and desmosomal proteins indicate cell type heterogeneity  
1053 and pluripotential differentiation. *Am J Pathol* **127**, 288-304 (1987).
- 1054 62. S. Lizard-Nacol, G. Lizard, E. Justrabo, C. Turc-Carel, Immunologic  
1055 characterization of Ewing's sarcoma using mesenchymal and neural markers. *Am*  
1056 *J Pathol* **135**, 847-855 (1989).
- 1057 63. S. Lizard-Nacol, C. Volk, G. Lizard, C. Turc-Carel, Abnormal expression of  
1058 neurofilament proteins in Ewing's sarcoma cell cultures. *Tumour Biol* **13**, 36-43  
1059 (1992).
- 1060 64. S. Kailayangiri, B. Altvater, S. Lesch, S. Balbach, C. Göttlich, J. Kühnemundt, J.  
1061 H. Mikesch, S. Schelhaas, S. Jamitzky, J. Meltzer, N. Farwick, L. Greune, M.  
1062 Fluegge, K. Kerl, H. N. Lode, N. Siebert, I. Müller, H. Walles, W. Hartmann, C.  
1063 Rossig, EZH2 Inhibition in Ewing Sarcoma Upregulates G(D2) Expression for  
1064 Targeting with Gene-Modified T Cells. *Mol. Ther.* **27**, 933-946 (2019).

- 1065 65. M. A. Krook, A. G. Hawkins, R. M. Patel, D. R. Lucas, R. Van Noord, R. Chugh,  
1066 E. R. Lawlor, A bivalent promoter contributes to stress-induced plasticity of  
1067 CXCR4 in Ewing sarcoma. *Oncotarget* **7**, 61775-61788 (2016).
- 1068 66. K. E. Ryland, L. K. Svoboda, E. D. Vesely, J. C. McIntyre, L. Zhang, J. R.  
1069 Martens, E. R. Lawlor, Polycomb-dependent repression of the potassium channel-  
1070 encoding gene KCNA5 promotes cancer cell survival under conditions of stress.  
1071 *Oncogene* **34**, 4591-4600 (2015).
- 1072 67. S. Bender, Y. Tang, A. M. Lindroth, V. Hovestadt, D. T. W. Jones, M. Kool, M.  
1073 Zapatka, P. A. Northcott, D. Sturm, W. Wang, B. Radlwimmer, J. W. Højfeldt, N.  
1074 Truffaux, D. Castel, S. Schubert, M. Ryzhova, H. Şeker-Cin, J. Gronych, P. D.  
1075 Johann, S. Stark, J. Meyer, T. Milde, M. Schuhmann, M. Ebinger, C. M.  
1076 Monoranu, A. Ponnuswami, S. Chen, C. Jones, O. Witt, V. P. Collins, A. von  
1077 Deimling, N. Jabado, S. Puget, J. Grill, K. Helin, A. Korshunov, P. Lichter, M.  
1078 Monje, C. Plass, Y. J. Cho, S. M. Pfister, Reduced H3K27me3 and DNA  
1079 Hypomethylation Are Major Drivers of Gene Expression in K27M Mutant  
1080 Pediatric High-Grade Gliomas. *Cancer Cell* **24**, 660-672 (2013).
- 1081 68. G. P. Souroullas, W. R. Jeck, J. S. Parker, J. M. Simon, J. Y. Liu, J. Paulk, J.  
1082 Xiong, K. S. Clark, Y. Fedoriw, J. Qi, C. E. Burd, J. E. Bradner, N. E. Sharpless,  
1083 An oncogenic Ezh2 mutation induces tumors through global redistribution of  
1084 histone 3 lysine 27 trimethylation. *Nat. Med.* **22**, 632-640 (2016).
- 1085 69. E. A. Pedersen, R. Menon, K. M. Bailey, D. G. Thomas, R. A. Van Noord, J. Tran,  
1086 H. Wang, P. P. Qu, A. Hoering, E. R. Fearon, R. Chugh, E. R. Lawlor, Activation  
1087 of Wnt/ $\beta$ -Catenin in Ewing Sarcoma Cells Antagonizes EWS/ETS Function and  
1088 Promotes Phenotypic Transition to More Metastatic Cell States. *Cancer Res.* **76**,  
1089 5040-5053 (2016).
- 1090 70. M. H. Bailey, C. Tokheim, E. Porta-Pardo, S. Sengupta, D. Bertrand, A.  
1091 Weerasinghe, A. Colaprico, M. C. Wendl, J. Kim, B. Reardon, P. K. Ng, K. J.  
1092 Jeong, S. Cao, Z. Wang, J. Gao, Q. Gao, F. Wang, E. M. Liu, L. Mularoni, C.  
1093 Rubio-Perez, N. Nagarajan, I. Cortés-Ciriano, D. C. Zhou, W. W. Liang, J. M.  
1094 Hess, V. D. Yellapantula, D. Tamborero, A. Gonzalez-Perez, C. Suphavitai, J. Y.  
1095 Ko, E. Khurana, P. J. Park, E. M. Van Allen, H. Liang, M. S. Lawrence, A.  
1096 Godzik, N. Lopez-Bigas, J. Stuart, D. Wheeler, G. Getz, K. Chen, A. J. Lazar, G.  
1097 B. Mills, R. Karchin, L. Ding, Comprehensive Characterization of Cancer Driver  
1098 Genes and Mutations. *Cell* **173**, 371-385. (2018).
- 1099 71. J. Andricovich, S. Perkail, Y. Kai, N. Casasanta, W. Peng, A. Tzatsos, Loss of  
1100 KDM6A Activates Super-Enhancers to Induce Gender-Specific Squamous-like  
1101 Pancreatic Cancer and Confers Sensitivity to BET Inhibitors. *Cancer Cell* **33**,  
1102 512-526.e518 (2018).
- 1103 72. X. Li, Y. Zhang, L. Zheng, M. Liu, C. D. Chen, H. Jiang, UTX is an escape from  
1104 X-inactivation tumor-suppressor in B cell lymphoma. *Nat Commun* **9**, 2720  
1105 (2018).
- 1106 73. G. Robinson, M. Parker, T. A. Kranenburg, C. Lu, X. Chen, L. Ding, T. N.  
1107 Phoenix, E. Hedlund, L. Wei, X. Zhu, N. Chalhoub, S. J. Baker, R. Huether, R.  
1108 Kriwacki, N. Curley, R. Thiruvankatam, J. Wang, G. Wu, M. Rusch, X. Hong, J.  
1109 Becksfort, P. Gupta, J. Ma, J. Easton, B. Vadodaria, A. Onar-Thomas, T. Lin, S.  
1110 Li, S. Pounds, S. Paugh, D. Zhao, D. Kawauchi, M. F. Roussel, D. Finkelstein, D.  
1111 W. Ellison, C. C. Lau, E. Bouffet, T. Hassall, S. Gururangan, R. Cohn, R. S.  
1112 Fulton, L. L. Fulton, D. J. Dooling, K. Ochoa, A. Gajjar, E. R. Mardis, R. K.  
1113 Wilson, J. R. Downing, J. Zhang, R. J. Gilbertson, Novel mutations target distinct  
1114 subgroups of medulloblastoma. *Nature* **488**, 43-48 (2012).



- 1115 74. S.-H. Lee, O. Kim, H.-J. Kim, C. Hwangbo, J.-H. Lee, Epigenetic regulation of  
1116 TGF-beta-induced EMT by JMJD3/KDM6B histone H3K27 demethylase.  
1117 *Oncogenesis* **10**, 17 (2021).
- 1118 75. S. Ramadoss, X. Chen, C.-Y. Wang, Histone demethylase KDM6B promotes  
1119 epithelial-mesenchymal transition. *J. Biol. Chem.* **287**, 44508-44517 (2012).
- 1120 76. J. H. Kim, A. Sharma, S. S. Dhar, S. H. Lee, B. Gu, C. H. Chan, H. K. Lin, M. G.  
1121 Lee, UTX and MLL4 coordinately regulate transcriptional programs for cell  
1122 proliferation and invasiveness in breast cancer cells. *Cancer Res.* **74**, 1705-1717  
1123 (2014).
- 1124 77. Q.-Y. Tang, S.-F. Zhang, S.-K. Dai, C. Liu, Y.-Y. Wang, H.-Z. Du, Z.-Q. Teng,  
1125 C.-M. Liu, UTX Regulates Human Neural Differentiation and Dendritic  
1126 Morphology by Resolving Bivalent Promoters. *Stem Cell Reports* **15**, 439-453  
1127 (2020).
- 1128 78. R. Hashizume, N. Andor, Y. Ihara, R. Lerner, H. Gan, X. Chen, D. Fang, X.  
1129 Huang, M. W. Tom, V. Ngo, D. Solomon, S. Mueller, P. L. Paris, Z. Zhang, C.  
1130 Petritsch, N. Gupta, T. A. Waldman, C. D. James, Pharmacologic inhibition of  
1131 histone demethylation as a therapy for pediatric brainstem glioma. *Nat. Med.* **20**,  
1132 1394-1396 (2014).
- 1133 79. T. L. Lochmann, K. M. Powell, J. Ham, K. V. Floros, D. A. R. Heisey, R. I. J.  
1134 Kurupi, M. L. Calbert, M. S. Ghotra, P. Greninger, M. Dozmorov, M. Gowda, A.  
1135 J. Souers, C. P. Reynolds, C. H. Benes, A. C. Faber, Targeted inhibition of histone  
1136 H3K27 demethylation is effective in high-risk neuroblastoma. *Sci Transl Med* **10**,  
1137 eaao4680 (2018).
- 1138 80. D. A. R. Heisey, S. Jacob, T. L. Lochmann, R. Kurupi, M. S. Ghotra, M. L.  
1139 Calbert, M. Shende, Y. K. Maves, J. E. Koblinski, M. G. Dozmorov, S. A. Boikos,  
1140 C. H. Benes, A. C. Faber, Pharmaceutical Interference of the EWS-FLI1-driven  
1141 Transcriptome By Cotargeting H3K27ac and RNA Polymerase Activity in Ewing  
1142 Sarcoma. *Mol. Cancer Ther.* **20**, 1868-1879 (2021).
- 1143 81. M. Vicioso-Mantis, R. Fueyo, C. Navarro, S. Cruz-Molina, W. F. J. van Ijcken,  
1144 E. Rebollo, Á. Rada-Iglesias, M. A. Martínez-Balbás, JMJD3 intrinsically  
1145 disordered region links the 3D-genome structure to TGFβ-dependent transcription  
1146 activation. *Nat. Commun.* **13**, 3263 (2022).
- 1147 82. B. Shi, W. Li, Y. Song, Z. Wang, R. Ju, A. Ulman, J. Hu, F. Palomba, Y. Zhao, J.  
1148 P. Le, W. Jarrard, D. Dimoff, M. A. Digman, E. Gratton, C. Zang, H. Jiang, UTX  
1149 condensation underlies its tumour-suppressive activity. *Nature* **597**, 726-731  
1150 (2021).
- 1151 83. T. Ezponda, D. Dupéré-Richer, C. M. Will, E. C. Small, N. Varghese, T. Patel, B.  
1152 Nabet, R. Popovic, J. Oyer, M. Bulic, Y. Zheng, X. Huang, M. Y. Shah, S. Maji,  
1153 A. Riva, M. Occhionorelli, G. Tonon, N. Kelleher, J. Keats, J. D. Licht,  
1154 UTX/KDM6A Loss Enhances the Malignant Phenotype of Multiple Myeloma and  
1155 Sensitizes Cells to EZH2 inhibition. *Cell Rep* **21**, 628-640 (2017).
- 1156 84. L. D. Ler, S. Ghosh, X. Chai, A. A. Thike, H. L. Heng, E. Y. Siew, S. Dey, L. K.  
1157 Koh, J. Q. Lim, W. K. Lim, S. S. Myint, J. L. Loh, P. Ong, X. X. Sam, D. Huang,  
1158 T. Lim, P. H. Tan, S. Nagarajan, C. W. S. Cheng, H. Ho, L. G. Ng, J. Yuen, P.-H.  
1159 Lin, C.-K. Chuang, Y.-H. Chang, W.-H. Weng, S. G. Rozen, P. Tan, C. L. Creasy,  
1160 S.-T. Pang, M. T. McCabe, S. L. Poon, B. T. Teh, Loss of tumor suppressor  
1161 KDM6A amplifies PRC2-regulated transcriptional repression in bladder cancer  
1162 and can be targeted through inhibition of EZH2. *Sci Transl Med* **9**, eaai8312  
1163 (2017).

- 1164 85. Q. Wu, Y. Tian, J. Zhang, X. Tong, H. Huang, S. Li, H. Zhao, Y. Tang, C. Yuan,  
1165 K. Wang, Z. Fang, L. Gao, X. Hu, F. Li, Z. Qin, S. Yao, T. Chen, H. Chen, G.  
1166 Zhang, W. Liu, Y. Sun, L. Chen, K. K. Wong, K. Ge, L. Chen, H. Ji, In vivo  
1167 CRISPR screening unveils histone demethylase UTX as an important epigenetic  
1168 regulator in lung tumorigenesis. *Proc. Natl. Acad. Sci. U.S.A* **115**, E3978-e3986  
1169 (2018).
- 1170 86. L. Chen, G. Alexe, N. V. Dharia, L. Ross, A. B. Iniguez, A. S. Conway, E. J.  
1171 Wang, V. Veschi, N. Lam, J. Qi, W. C. Gustafson, N. Nasholm, F. Vazquez, B.  
1172 A. Weir, G. S. Cowley, L. D. Ali, S. Pantel, G. Jiang, W. F. Harrington, Y. Lee,  
1173 A. Goodale, R. Lubonja, J. M. Krill-Burger, R. M. Meyers, A. Tsherniak, D. E.  
1174 Root, J. E. Bradner, T. R. Golub, C. W. Roberts, W. C. Hahn, W. A. Weiss, C. J.  
1175 Thiele, K. Stegmaier, CRISPR-Cas9 screen reveals a MYCN-amplified  
1176 neuroblastoma dependency on EZH2. *J. Clin. Invest.* **128**, 446-462 (2018).
- 1177 87. J. K. Parrish, T. S. McCann, M. Sechler, L. M. Sobral, W. Ren, K. L. Jones, A. C.  
1178 Tan, P. Jedlicka, The Jumonji-domain histone demethylase inhibitor JIB-04  
1179 deregulates oncogenic programs and increases DNA damage in Ewing Sarcoma,  
1180 resulting in impaired cell proliferation and survival, and reduced tumor growth.  
1181 *Oncotarget* **9**, 33110-33123 (2018).
- 1182 88. D. Suva, G. Garavaglia, J. Menetrey, B. Chapuis, P. Hoffmeyer, L. Bernheim, V.  
1183 Kindler, Non-hematopoietic human bone marrow contains long-lasting,  
1184 pluripotential mesenchymal stem cells. *J Cell Physiol* **198**, 110-118 (2004).
- 1185 89. D. Suva, J. Passweg, S. Arnaudeau, P. Hoffmeyer, V. Kindler, In vitro activated  
1186 human T lymphocytes very efficiently attach to allogenic multipotent  
1187 mesenchymal stromal cells and transmigrate under them. *J Cell Physiol* **214**, 588-  
1188 594 (2008).
- 1189 90. D. Conant, T. Hsiau, N. Rossi, J. Oki, T. Maures, K. Waite, J. Yang, S. Joshi, R.  
1190 Kelso, K. Holden, B. L. Enzmann, R. Stoner, Inference of CRISPR Edits from  
1191 Sanger Trace Data. *Crispr j* **5**, 123-130 (2022).
- 1192 91. C. A. Schneider, W. S. Rasband, K. W. Eliceiri, NIH Image to ImageJ: 25 years  
1193 of image analysis. *Nat. Methods* **9**, 671-675 (2012).
- 1194 92. C. Guzmán, M. Bagga, A. Kaur, J. Westermarck, D. Abankwa, ColonyArea: an  
1195 ImageJ plugin to automatically quantify colony formation in clonogenic assays.  
1196 *PloS one* **9**, e92444 (2014).
- 1197 93. S. W. Wingett, S. Andrews, FastQ Screen: A tool for multi-genome mapping and  
1198 quality control. *F1000Res* **7**, 1338 (2018).
- 1199 94. M. Martin, Cutadapt removes adapter sequences from high-throughput  
1200 sequencing reads. *EMBnet j.* **17**, (2011).
- 1201 95. N. L. Bray, H. Pimentel, P. I. Melsted, L. Pachter, Near-optimal probabilistic  
1202 RNA-seq quantification. *Nat. Biotechnol.* **34**, 525--527 (2016).
- 1203 96. C. Sonesson, M. I. Love, M. D. Robinson, Differential analyses for RNA-seq:  
1204 transcript-level estimates improve gene-level inferences. *F1000Res* **4**, 1521  
1205 (2015).
- 1206 97. M. I. Love, W. Huber, S. Anders, Moderated estimation of fold change and  
1207 dispersion for RNA-seq data with DESeq2. *Genome Biol.* **15**, 550 (2014).
- 1208 98. M. E. Ritchie, B. Phipson, D. Wu, Y. Hu, C. W. Law, W. Shi, G. K. Smyth, limma  
1209 powers differential expression analyses for RNA-sequencing and microarray  
1210 studies. *Nucleic Acids Res.* **43**, e47--e47 (2015).
- 1211 99. A. Subramanian, P. Tamayo, V. K. Mootha, S. Mukherjee, B. L. Ebert, M. A.  
1212 Gillette, A. Paulovich, S. L. Pomeroy, T. R. Golub, E. S. Lander, J. P. Mesirov,  
1213 Gene set enrichment analysis: A knowledge-based approach for interpreting

- 1214 genome-wide expression profiles. *Proc. Natl. Acad. Sci. U.S.A* **102**, 15545-15550  
1215 (2005).
- 1216 100. M. V. Kuleshov, M. R. Jones, A. D. Rouillard, N. F. Fernandez, Q. Duan, Z.  
1217 Wang, S. Koplev, S. L. Jenkins, K. M. Jagodnik, A. Lachmann, M. G.  
1218 McDermott, C. D. Monteiro, G. W. Gundersen, A. Ma'ayan, Enrichr: a  
1219 comprehensive gene set enrichment analysis web server 2016 update. *Nucleic  
1220 Acids Res.* **44**, W90-W97 (2016).
- 1221 101. S. Detre, G. Saclani Jotti, M. Dowsett, A "quickscore" method for  
1222 immunohistochemical semiquantitation: validation for oestrogen receptor in  
1223 breast carcinomas. *J. Clin. Pathol.* **48**, 876-878 (1995).
- 1224 102. F. Varghese, A. B. Bukhari, R. Malhotra, A. De, IHC Profiler: an open source  
1225 plugin for the quantitative evaluation and automated scoring of  
1226 immunohistochemistry images of human tissue samples. *PloS one* **9**, e96801  
1227 (2014).
- 1228 103. S. Sánchez-Molina, C. Estarás, J. L. Oliva, N. Akizu, E. Asensio-Juan, J. M.  
1229 Rojas, M. A. Martínez-Balbás, Regulation of CBP and Tip60 coordinates histone  
1230 acetylation at local and global levels during Ras-induced transformation.  
1231 *Carcinogenesis* **35**, 2194-2202 (2014).
- 1232 104. B. Langmead, C. Trapnell, M. Pop, S. L. Salzberg, Ultrafast and memory-efficient  
1233 alignment of short DNA sequences to the human genome. *Genome Biol.* **10**, R25  
1234 (2009).
- 1235 105. Y. Zhang, T. Liu, C. A. Meyer, J. Eeckhoutte, D. S. Johnson, B. E. Bernstein, C.  
1236 Nusbaum, R. M. Myers, M. Brown, W. Li, X. S. Liu, Model-based Analysis of  
1237 ChIP-Seq (MACS). *Genome Biol.* **9**, R137 (2008).
- 1238 106. C. S. Ross-Innes, R. Stark, A. E. Teschendorff, K. A. Holmes, H. R. Ali, M. J.  
1239 Dunning, G. D. Brown, O. Gojis, I. O. Ellis, A. R. Green, S. Ali, S.-F. Chin, C.  
1240 Palmieri, C. Caldas, J. S. Carroll, Differential oestrogen receptor binding is  
1241 associated with clinical outcome in breast cancer. *Nature* **481**, 389-393 (2012).
- 1242 107. E. Blanco, M. González-Ramírez, L. Di Croce, Productive visualization of high-  
1243 throughput sequencing data using the SeqCode open portable platform. *Sci Rep*  
1244 **11**, 19545 (2021).
- 1245 108. N. A. O'Leary, M. W. Wright, J. R. Brister, S. Ciuffo, D. Haddad, R. McVeigh, B.  
1246 Rajput, B. Robbertse, B. Smith-White, D. Ako-Adjei, A. Astashyn, A. Badretdin,  
1247 Y. Bao, O. Blinkova, V. Brover, V. Chetvernin, J. Choi, E. Cox, O. Ermolaeva,  
1248 C. M. Farrell, T. Goldfarb, T. Gupta, D. Haft, E. Hatcher, W. Hlavina, V. S.  
1249 Joardar, V. K. Kodali, W. Li, D. Maglott, P. Masterson, K. M. McGarvey, M. R.  
1250 Murphy, K. O'Neill, S. Pujar, S. H. Rangwala, D. Rausch, L. D. Riddick, C.  
1251 Schoch, A. Shkeda, S. S. Storz, H. Sun, F. Thibaud-Nissen, I. Tolstoy, R. E. Tully,  
1252 A. R. Vatsan, C. Wallin, D. Webb, W. Wu, M. J. Landrum, A. Kimchi, T.  
1253 Tatusova, M. DiCuccio, P. Kitts, T. D. Murphy, K. D. Pruitt, Reference sequence  
1254 (RefSeq) database at NCBI: current status, taxonomic expansion, and functional  
1255 annotation. *Nucleic Acids Res.* **44**, D733-745 (2016).
- 1256 109. W. J. Kent, C. W. Sugnet, T. S. Furey, K. M. Roskin, T. H. Pringle, A. M. Zahler,  
1257 D. Haussler, The human genome browser at UCSC. *Genome Res.* **12**, 996-1006  
1258 (2002).
- 1259 110. P. Machanick, T. L. Bailey, MEME-ChIP: motif analysis of large DNA datasets.  
1260 *Bioinformatics* **27**, 1696-1697 (2011).

**Acknowledgements:** we thank M. Martínez-Balbás for critical reading of the manuscript.

We also thank M. Suñol, Sandra Rincón and Neus Prats for technical advice. Last, we are

grateful to the Band of Parents at Hospital Sant Joan de Déu for supporting the overall research activities of the Pediatric Cancer Group (IRSJD and PCCB).

**Funding:** The work in the J.M. laboratory is supported by grants from AGAUR and Instituto de Salud Carlos III. E.F.-B. was supported by the Spanish government grant, Instituto de Salud Carlos III (PI16/00245) to J.M. The work in the L.D.C. laboratory is supported by grants from the Spanish Economy, Industry and Competitiveness (MEIC) (PID2019-108322GB-100) Ministry and from AGAUR.

**Author contributions:** E.F.-B, S.S.-M. and J. M. designed and wrote the manuscript. S.S.-M. and J.M. supervised all the work conducted. E.F.-B., C. R., M.S.-J., P.T., O.M., E.P. and S.M. performed the experiments. E.B., G.F., P.C, S.P. and S.G. performed all the statistical and bioinformatic analysis. N.R., A.A., C.L., and L.dC provided expertise and feedback. All authors reviewed the manuscript.

**Competing interests:** Authors declare that they have no competing interests.

**Data and materials availability:** All data needed to evaluate the conclusions in the paper are present in the paper and/or the Supplementary Materials. The RNA-seq and ChIP-seq data generated in this article were deposited in the National Center for Biotechnology Information Gene Expression Omnibus (NCBI GEO) repository under the accession number GSE211743.

## 1261 **Figures and Tables**

1262 **Fig. 1. H3K27me3 genome-wide redistribution upon EWSR1-FLI1 overexpression**  
1263 **in hpMSCs. (A)** Western blot showing levels of FLI1 and H3K27me3 in whole cell and  
1264 histone extracts, respectively, in control (CTRL) and upon EWSR1-FLI1 overexpression  
1265 in hpMSC (EF). Tubulin and histone H4 were used as loading controls. Numbers below  
1266 represent band quantification of H3K27me3 normalized to H4 and relative to CTRL. **(B)**  
1267 Heatmap depicting H3K27me3 and EWSR1-FLI1 ChIP-seq in 4,080 H3K27me3-FLI1  
1268 coinciding bins for CTRL and EWSR1-FLI1 hpMSC. **(C)** Ranking of genes associated  
1269 to H3K27me3 signal strength in bins (red for genes gaining and blue for genes losing  
1270 H3K27me3) upon EWSR1-FLI1 overexpression in hpMSC. **(D)** University of California  
1271 Santa Cruz (UCSC) genome browser signal tracks for H3K27me3, H3K27ac, and FLI1  
1272 in CTRL and EWSR1-FLI1 hpMSC at the *NKX2-2* gene. Up or Down bins correspond to  
1273 regions that gain or loss H3K27me3 upon EWSR1-FLI1 introduction, respectively, and  
1274 are represented as black rectangles below tracks. Clusters of bins are highlighted in light  
1275 blue. **(E)** Same as (D), at the *TGFBI* gene. **(F)** Violin plots representing mRNA levels of

1276 KDM6A (above) and KDM6B (below) in a panel of EwS, osteosarcoma (OS),  
1277 rhabdomyosarcoma (RMS), and synovial sarcoma (SS) cell lines extracted from Barretina  
1278 *et al.*(45). (G) Same as (F) in primary sarcoma tumors from NCBI GEO public repository.  
1279 MSCs derived from a healthy bone marrow were used as control tissue. (H)  
1280 Immunohistochemical staining of KDM6A (above) and KDM6B (below) on sections of  
1281 three representative primary EwS tumors from the cohort of 43 tumors from our  
1282 institution counterstained with hematoxylin-eosin. White bar indicates 100 $\mu$ m scale.  
1283 Statistical significance was determined by one-way analysis of variance (ANOVA) test  
1284 with Holm-Šídák multiple comparison test (F) and (G) relative to EwS. \*\*\*\*  $P < 0,0001$ ,  
1285 \*\* $P < 0.01$ , and \* $P < 0.05$ .

1286 **Fig. 2. KDM6A and KDM6B co-localize genome-wide with EWSR1-FLI1 at primed**  
1287 **and active enhancers.** (A) Pie chart showing genomic distribution of KDM6A, KDM6B,  
1288 and EWSR1-FLI1 peaks relative to functional categories including promoters ( $\pm 2.5$ kb  
1289 from TSS), genic regions (intragenic regions not overlapping with promoter) and  
1290 intergenic regions (rest of the genome) in A673 cells. (B) Bar plot depicting percentage  
1291 of total regulatory elements in the genome (active/poised/primed enhancers and  
1292 active/poised promoters) overlapping with KDM6A, KDM6B, and EWSR1-FLI1 peaks.  
1293 (C) Venn diagram depicting the overlap of KDM6A, KDM6B, and EWSR1-FLI1 peaks  
1294 in A673 cells. Table below shows top MEME DNA motifs and the corresponding E-value  
1295 for every group of peaks. (D) Boxplots depicting the average ChIP-seq signal of H3K27ac  
1296 (above) and H3K4me1 (below) on each subset of peaks. (E) Heatmap of KDM6A,  
1297 KDM6B, EWSR1-FLI1, H3K27ac, H3K4me3, and H3K4me1 ChIP-seq signals for each  
1298 group of peaks. (F) UCSC genome browser signal tracks for KDM6A, KDM6B, EWSR1-  
1299 FLI1, H3K27ac, and H3K4me1 in A673 cells at the *CDH11* enhancer (above), and the  
1300 *NKX2-2* enhancer (below). EWSR1-FLI1-KDM6B peaks with or without KDM6A (A-  
1301 B-EF or B-EF, respectively) are represented as black bars below tracks. Statistical  
1302 significance was determined by Wilcoxon signed-rank test relative to KDM6B-EF peaks  
1303 (D). Error bars in (D) indicate SD. \*\*\*\*  $P < 0,0001$

1304 **Fig. 3. Knockdown of KDM6A and KDM6B downregulates EWSR1-FLI1-activated**  
1305 **targets.** (A) Boxplot depicting the average ChIP-seq signal of Flag, EWSR1-FLI1,  
1306 KDM6A and KDM6B at EWSR1-FLI1 induced peaks before (HeLa) and upon induction  
1307 of the oncogene (iHeLa). (B) Aggregated plot showing the average ChIP-seq signal of  
1308 EWSR1-FLI1, KDM6A and KDM6B at EWSR1-FLI1 peaks in control and induced Hela  
1309 cells. (C) Boxplot representing the RNA-seq levels in A673 cells of KDM6A, KDM6B,  
1310 and EWSR1-FLI1 target genes from Riggi *et al.* (16). (D) Western blot showing levels of  
1311 KDM6A and KDM6B in whole cell extracts upon KDM6A (left) or KDM6B (right)  
1312 knockdown with two shRNA sequences (sh#1 and sh#2) at 72 hours doxycycline-  
1313 induction in A673 cells. Tubulin was used as loading control. Numbers below represent  
1314 band quantification of KDM6A or KDM6B normalized to tubulin and relative to  
1315 shCTRL. (E) Gene Set Enrichment Analysis (GSEA) curves and Normalized Enrichment  
1316 Scores (NES) for Hallmark collection of Epithelial to Mesenchymal Transition (EMT) in  
1317 targets downregulated upon shKDM6A#2 (above) and shKDM6B#2 (below) knockdown

1318 in A673 cells. False Discovery Rate (FDR) is also shown. (F) Heatmap and dendrogram  
 1319 showing expression levels of genes in the vicinity (100 kb) of KDM6A-EWSR1-FLI1  
 1320 (left) and KDM6B-EWSR1-FLI1 (right) ChIP-seq peaks significantly downregulated  
 1321 upon knockdown of each demethylase in A673 cells. n, indicates number of deregulated  
 1322 direct targets upon knockdown. (G) UCSC genome browser signal tracks for KDM6A,  
 1323 KDM6B, EWSR1-FLI1, and H3K27ac at *SYT1* gene. RNA-seq tracks for shKDM6A  
 1324 (shRNA#2) and shKDM6B (shRNA#2) and the corresponding shCTRL in A673 are  
 1325 shown. (H) Same as (F) at *IGF1* gene. Statistical significance between groups was  
 1326 assessed by Wilcoxon signed-rank test (C). Error bars in (A and C) indicate SD of  
 1327 RPKMs. \*\*\* P<0,001

1328 **Fig. 4. KDM6A recruits BRG1 to EWSR1-FLI1-activated enhancers in a**  
 1329 **demethylase-independent manner.** (A) Western blot of KDM6A, KDM6B, and  
 1330 EWSR1-FLI1 in whole cell extracts upon KDM6A KO with two sgRNA sequences (#1  
 1331 and #2) in A673 cells. Tubulin was used as loading control. (B) Heatmap showing  
 1332 expression levels of significantly downregulated genes in the vicinity (100 kb) of  
 1333 KDM6A-EWSR1-FLI1 ChIP-seq peaks upon sgKDM6A#1 and #2 in A673 cells. (C)  
 1334 RT-qPCR of KDM6B-EWSR1-FLI1 targets with or without KDM6A ChIP-seq peaks in  
 1335 A673 sgKDM6A#1 and #2. (D) Boxplot depicting the average ChIP-seq signal of  
 1336 H3K27me3 at 4,369 peaks exclusive for sgCTRL or 1,616 peaks for sgKDM6A#1  
 1337 (sgCTRL<sup>+</sup>/sgKDM6A<sup>-</sup> and sgCTRL<sup>-</sup>/sgKDM6A<sup>+</sup>, respectively), and 1,610 peaks in  
 1338 common (sgCTRL<sup>+</sup>/sgKDM6A<sup>+</sup>). (E) Venn diagram depicting genes associated to  
 1339 H3K27me3 peaks in sgCTRL and sgKDM6A#1. (F) UCSC genome browser signal tracks  
 1340 for H3K27me3 at *SYT1* intronic enhancer in sgCTRL and sgKDM6A#1. (G) RT-qPCR  
 1341 of EWSR1/FLI1-KDM6A targets with (left) or without KDM6B (middle) in A673  
 1342 sgKDM6A#1 upon overexpression of KDM6A WT or dead mutant (H1146A/E1148A).  
 1343 (H) Venn diagram depicting the overlap between KDM6A-EWSR1-FLI1 and BRG1  
 1344 peaks in A673 cells. (I) Boxplot of BRG1 ChIP-seq signal on the common set of 1808  
 1345 KDM6A-EWSR1-FLI1 and BRG1 peaks upon sgKDM6A#1. (J) ChIP-qPCR of BRG1,  
 1346 KDM6A, and H3K27me3 enrichment at the enhancer and promoter region of *IRS2* and  
 1347 *SYT1* KDM6A-activated targets upon sgKDM6A#1. *DICER* was used as a negative  
 1348 control region. Wilcoxon signed-rank test (D), Kruskal-Wallis test with Dunn's  
 1349 correction relative to sgCTRL (C) and (G), two-tailed Mann-Whitney test relative to  
 1350 sgKDM6A#1 (G), and ordinary two-way ANOVA with Holm-Šidák test relative to  
 1351 control (J) were applied. *GAPDH* was used as housekeeping gene (C) and (G). Error bars  
 1352 indicate SEM (C), (G) and (J) of three independent biological experiments and SD  
 1353 (D) and (I); \*\*\*\*P<0.0001, \*\*P < 0.01, and \*P < 0.05.

1354 **Fig. 5. KDM6A knockout decreases EwS tumor growth.** (A) Colony formation assay  
 1355 of KDM6A KO cells (sgRNA#1 and 2) compared to parental cells and sgCTRL in A673.  
 1356 (B) Tumor growth curves of the average volume of xenografts derived from subcutaneous  
 1357 injection of KDM6A KO cells compared to parental and sgCTRL A673 cells in nude  
 1358 athymic mice (n=11 for parental, n=11 sgKDM6A#1, n=9 sgCTRL (left); n=9 for  
 1359 parental, n=7 sgKDM6A#2 and n=12 sgCTRL (right); n, indicates number of tumors).

1360 (C) RT-qPCR determination of KDM6A targets *CDH11* and *IRS2* in RNA extracts from  
1361 tumors excised from parental, sgCTRL and sgKDM6A (sgRNA#1) xenografts of A673  
1362 cells. *EWSR1-FLI1* and *KDM6A* expression is also shown. *GAPDH* was used as  
1363 housekeeping gene. (D) Kaplan-Meier representing the percentage of xenograft tumors  
1364 that reach a tumor volume of 1000 mm<sup>3</sup> within days post-injection in parental, sgCTRL  
1365 and KDM6A KO (sgRNA#1 and 2) in A673 cells. (E) Same as (D) representing the  
1366 percentage of xenograft tumors that reach a tumor volume of 150 mm<sup>3</sup>. (F)  
1367 Immunohistochemistry staining of CD99, KDM6A, Ki67, and NF200 on sections of  
1368 tumors excised from sgCTRL and sgKDM6A (sgRNA#1) xenografts of A673 cells.  
1369 CD99 was used as positive control for EwS cells, Ki67 for cell proliferation, and  
1370 hematoxylin-eosin for histopathological evaluation of tissue. White scale bar represents  
1371 50 μm. Statistical significance was determined by Kruskal-Wallis test with Dunn's  
1372 multiple comparison correction (C) relative to sgCTRL. Survival analysis was performed  
1373 by Log-rank (Mantel Cox) test (D, E) relative to sgCTRL. Error bars indicate SEM of  
1374 xenografts (B) and four independent xenograft tumors (C). \*\*\**P*<0.001, \*\**P* < 0.01,  
1375 and \**P* < 0.05.

1376 **Fig. 6. Impact of KDM6B knockout in EWSR1-FLI1 targets.** (A) Western blot  
1377 showing levels of KDM6A, KDM6B, and EWSR1-FLI1 in whole cell extracts upon  
1378 KDM6B KO with two sgRNA sequences (#1 and #2) in A673 cells. Tubulin was used as  
1379 loading control. (B) Heatmap showing expression levels of significantly downregulated  
1380 genes in the vicinity (100 kb) of KDM6B-EWSR1-FLI1 ChIP-seq peaks upon  
1381 sgKDM6B#1 and #2 in A673 cells. (C) RT-qPCR of KDM6B-EWSR1-FLI1 targets with  
1382 or without KDM6A ChIP-seq peaks in A673 sgKDM6B#1 and #2. *GAPDH* was used as  
1383 housekeeping gene. (D) Boxplot depicting the average ChIP-seq signal of H3K27me3 at  
1384 3,248 peaks exclusive for sgCTRL or 2,366 peaks for sgKDM6B#2  
1385 (sgCTRL<sup>+</sup>/sgKDM6B<sup>-</sup> and sgCTRL<sup>-</sup>/sgKDM6B<sup>+</sup>, respectively), and 3,473 peaks in  
1386 common (sgCTRL<sup>+</sup>/sgKDM6B<sup>+</sup>). (E) Venn diagram depicting the overlap between genes  
1387 associated to H3K27me3 peaks in sgCTRL and sgKDM6B#2. (F) UCSC genome  
1388 browser signal tracks for H3K27me3 at the intronic enhancer of *JARID2* in sgCTRL and  
1389 sgKDM6B#2. (G) ChIP-qPCR of H3K27me3 enrichment at the enhancer region of  
1390 *NKX2-2* and *CCND1* genes upon KDM6B KO with sgRNA#2. *ENC1* was used as  
1391 negative control regions. (H) Venn diagram depicting the overlap of KDM6B-EWSR1-  
1392 FLI1 and BRG1 peaks in A673 cells. Statistical significance was determined by Kruskal-  
1393 Wallis test with Dunn's multiple comparison correction relative to sgCTRL (C),  
1394 Wilcoxon signed-rank test (D), and ordinary two-way ANOVA with Dunnett multiple  
1395 comparisons test relative to IgG (G). Error bars indicate SEM (C) and (G) of three  
1396 independent biological experiments or SD (D); \*\*\*\**P*<0.0001, \*\**P* < 0.01 and  
1397 \**P*<0.05.

1398 **Fig. 7. KDM6B knockout decreases tumor growth and sensitizes EwS cells to the**  
1399 **EZH2 inhibitor GSK126.** (A) Colony formation assay of KDM6B KO cells (sgRNA#1  
1400 and 2) compared to parental and sgCTRL A673 cells. (B) Tumor growth curve of the  
1401 average volume of xenografts derived from subcutaneous injection of KDM6B KO cells

1402 (sgRNA#1 and 2, n=11 each) compared to sgCTRL A673 cells (n=8, where n indicates  
1403 the number of tumors) in nude athymic mice. (C) Kaplan-Meier representing the  
1404 percentage of xenograft tumors that reach a tumor volume of 1000 mm<sup>3</sup> within days post-  
1405 injection in sgCTRL and KDM6B KO (sgRNA#1 and 2) in A673 cells. (D)  
1406 Immunohistochemistry staining of CD99, KDM6B, and Ki67 on sections of tumors  
1407 excised from sgCTRL and sgKDM6B (sgRNA#1 and sgRNA#2) xenografts of A673  
1408 cells. CD99 was used as positive control for EwS cells, Ki67 for cell proliferation, and  
1409 hematoxylin-eosin for histopathological evaluation of tissue. Black scale bar represents  
1410 50 μm. (E) Western blot showing levels of KDM6B, cleaved-PARP-1 (c-PARP), and  
1411 phosphorylation of S139 in variant gamma-H2A.x (γ-H2Ax) in whole cell extracts  
1412 (above) and H3K27me3 in histone extracts (below) from sgCTRL and sgKDM6B#2  
1413 A673 cells treated with vehicle or GSK126 inhibitor (15 μM for 24 hours). Tubulin and  
1414 histone H3 were used as loading controls, respectively. Numbers below represent band  
1415 quantification of H3K27me3 normalized to H3 and relative to sgCTRL or sgKDM6B#2  
1416 treated with vehicle. (F) Depletion of KDM6A, enriched at single GGAA regions bound  
1417 by EWSR1-FLI1, perturbs BRG1 recruitment causing repression of target genes in a  
1418 demethylase-independent manner (left). KDM6B co-localize with EWSR1-FLI1 and  
1419 BRG1 at GGAA repeats, where its depletion results in repression and a mild accumulation  
1420 of H3K27me3. Survival analysis was performed by Log-rank (Mantel Cox) test (C)  
1421 relative to sgCTRL. Error bars indicate SEM of xenografts (B). \*\*\*P<0.001 and  
1422 \*\*P<0.01.

## 1423 **Supplementary Materials**

1424 **Figure S1. H3K27me3 genome-wide redistribution upon EWSR1-FLI1**  
1425 **overexpression in hpMSCs.** (A) Metagene plot showing H3K27me3 (left) and H3K27ac  
1426 (right) ChIP-seq signals in 6,150 and 15,810 target genes, respectively, at transcription  
1427 start site (TSS) and transcription end sites (TES) within 5,000 kb window in control  
1428 (CTRL) and upon infection with the oncogene (EWSR1-FLI1) in hpMSC. (B) Scatter  
1429 plot of H3K27me3 signal in 3,069,655 bins of 1 kb in CTRL (x-axis) and EWSR1-FLI1  
1430 (y-axis) hpMSC (R<sup>2</sup>=0.582, slope=0.703). Bins that significantly gain (Up bins) or lose  
1431 H3K27me3 (Down bins) are highlighted in red or blue, respectively. (C) Boxplot  
1432 depicting the average ChIP-seq signal of H3K27me3 in Up and Down bins in CTRL and  
1433 EWSR1-FLI1 hpMSC. (D) Bar plot depicting percentage of annotated regulatory  
1434 elements (active/poised/primed enhancers and active/poised promoters) covered by at  
1435 least one bin of the genome (1 kb) in up bins or down bins of H3K27me3 in CTRL and  
1436 EWSR1-FLI1 hpMSC. (E) Bar chart representing the top five enriched signaling  
1437 pathways of 2,879 genes from Down bins (above) and 2,621 genes from Up bins (below)  
1438 from CTRL and EWSR1-FLI1 hpMSC and their associated P-value. (F) Boxplot  
1439 depicting immunohistochemical score (H-score) mean values for KDM6A and KDM6B  
1440 in our cohort of 45 EwS primary tumors (right). Individual H-score values are represented  
1441 as dots. Table shows descriptive statistics information of the recruited samples (left). (G)  
1442 Scatter plot of individual H-score values for KDM6A (x-axis) and KDM6B (y-axis)  
1443 (r=0.000, CI=(-0.308,0.308), P-value=1.00). Statistical differences between groups were  
1444 assessed by Wilcoxon signed-rank test (C). Error bars indicate SD (C) and (F).  
1445 P\*\*\*<0.001.



1446 **Figure S2. KDM6A and KDM6B co-localize genome-wide with EWSR1-FLI1 at**  
1447 **primed and active enhancers.** (A) Volcano plots of the significant peaks identified by  
1448 DiffBind for KDM6A, KDM6B, and EWSR1-FLI1 (3,737, 2,687, and 4,800  
1449 respectively) ( $P$  value  $\leq 0.05$  for KDM6A and EWSR1-FLI1, and  $FDR < 10^{-5}$  for  
1450 KDM6B) in A673 cells. (B) Table showing the top MEME DNA motifs enriched for  
1451 KDM6A, KDM6B and EWSR1-FLI1 peaks and the corresponding E-value for every set  
1452 of peaks. (C) Bar chart representing the top five enriched gene ontology (GO) biological  
1453 process of the 1,511 or 1,205 genes associated to KDM6A (above) or KDM6B peaks  
1454 (below), respectively, and their associated P-value. (D) Venn diagram showing overlap  
1455 of KDM6A, KDM6B, and EWSR1-FLI1 at peak level in TC71 cells. (E) Same as (D)  
1456 overlap between EWSR1-FLI1 and EZH2 at peak level in A673 cells. (F) Boxplot  
1457 depicting the average ChIP-seq signal of H3K4me3 (left) and H3K27me3 (right) in each  
1458 set of peaks in A673 cells. (G) Same as (F) showing the average ChIP-seq signal of  
1459 RING1B in each group of peaks in A673 cells. (H) UCSC genome browser signal tracks  
1460 for KDM6A, KDM6B, EWSR1-FLI1, H3K27ac, and H3K4me1 at the *SMYD3* gene in  
1461 A673. EWSR1-FLI1 and KDM6A peaks with or without KDM6B (A-B-EF or A-EF,  
1462 respectively) are represented as black bars below tracks. (I) ChIP-qPCR of KDM6A and  
1463 KDM6B in a set of EWSR1-FLI1-bound enhancer regions with both KDM6A and  
1464 KDM6B (A-B-EF) or only KDM6B (B-EF) in A673 cells. *ENCI* was used as a negative  
1465 control region. Statistical significance between groups was assessed by Wilcoxon signed-  
1466 rank test (F) and (G) and Kruskal-Wallis test with Dunn's correction for multiple  
1467 comparisons (I). Error bars indicate SD (F) and (G) or SEM of three independent  
1468 biological experiments (I). \*\*\*\* $P < 0.0001$ , \* $P < 0.05$  and ns indicates not significant.

1469 **Figure S3. Knockdown of KDM6A and KDM6B downregulates EWSR1-FLI1-**  
1470 **activated targets.** (A) Western blot showing levels of KDM6A and KDM6B in whole  
1471 cell extracts upon KDM6A (left) or KDM6B (right) knockdown with two doxycycline-  
1472 inducible shRNA sequences (sh#1 and sh#2) at 72 hours in TC71 cells. Tubulin was used  
1473 as loading control. Numbers below represent band intensity quantification of KDM6A or  
1474 KDM6B normalized to tubulin and relative to shCTRL. (B) Volcano plots depicting log  
1475 fold change (x-axis) and the associated log P-adjusted value (y-axis) of deregulated  
1476 targets upon KDM6A (left) or KDM6B (right) knockdown with #sh1 or #sh2 sequences  
1477 (above or below, respectively). Statistically significant deregulated targets according to  
1478 set cut-off are highlighted in red. (C) Donut charts representing the percentage of  
1479 significantly upregulated or downregulated targets upon KDM6A (above) or KDM6B  
1480 (below) knockdown with sh#1 and sh#2 in A673 cells (red; 492 and 502 genes for  
1481 shKDM6A#1 and #2, respectively; 1,090 and 1,369 genes for shKDM6B#1 and #2,  
1482 respectively) or TC71 cells (orange; 583 and 731 genes for shKDM6A#1 and #2,  
1483 respectively; 2,975 and 196 genes for shKDM6B#1 and #2, respectively). (D) Heatmap  
1484 showing expression levels of genes in the vicinity of KDM6A-EWSR1-FLI1 and  
1485 KDM6B-EWSR1-FLI1 ChIP-seq peaks (100 kb) that are significantly upregulated upon  
1486 knockdown of each demethylase in A673 cells. n, indicates number of deregulated direct  
1487 targets upon knockdown in each panel. (E) Bar chart representing the top five enriched  
1488 gene ontology (GO) biological process and their associated P-value of the 64 genes in the  
1489 vicinity (100 kb) of KDM6A-EWSR1-FLI1 peaks (above) and the 139 genes in the  
1490 vicinity (100 kb) of KDM6B-EWSR1-FLI1 peaks (below) that are significantly  
1491 downregulated upon knockdown of each demethylase in A673. (F) RT-qPCR  
1492 determination of mRNA expression of EWSR1-FLI1 targets with active enhancers in  
1493 shCTRL and shKDM6A (#1 and 2) in A673 cells. Values were normalized to *GAPDH*  
1494 and relative to shCTRL. (G) Same analysis as in (F) for shCTRL and shKDM6B (#1 and

1495 2) in A673 cells. Statistical significance was determined by Kruskal-Wallis test with  
1496 Dunn's multiple comparison correction related to sgCTRL. Error bars indicate SEM (F)  
1497 and (G) of four independent biological experiments. **\*\* $P < 0.01$ , and \* $P < 0.05$ .**

1498 **Figure S4. KDM6A recruits BRG1 to EWSR1-FLI1-activated enhancers in a**  
1499 **demethylase-independent manner.** (A) Western blot showing levels of H3K27ac,  
1500 H3K4me1, and H3K27me3 in histone extracts upon KDM6A KO with two sgRNA  
1501 sequences (#1 and #2) in A673 cells. Histone H3 was used as loading control. Numbers  
1502 below represent band quantification of H3K27me3 normalized to H3 and relative to non-  
1503 targeting control (sgCTRL). (B) Donut charts (up) representing the percentage of  
1504 significantly upregulated or downregulated targets upon KDM6A KO (red indicates  
1505 downregulated targets: 1,245 and 480 genes for sgKDM6A#1 and #2, respectively) in  
1506 A673 cells. Bar chart (below) representing the top five enriched gene ontology (GO)  
1507 biological process and their associated P-value of the set of differentially expressed genes  
1508 for KDM6A KO. (C) Western blot showing levels of KDM6A, and KDM6B in whole  
1509 cell extracts upon KDM6A KO with two sgRNA sequences (#1 and #2) in TC71 cells.  
1510 Tubulin was used as loading control. (D) RT-qPCR determination of EWSR1-FLI1  
1511 targets with both KDM6A and KDM6B ChIP-seq peaks (A-B-EF group) in TC71 KO  
1512 cells (sgRNA #1 and #2). *GAPDH* was used as housekeeping gene. (E) **Metagene plot**  
1513 **showing H3K27me3 ChIP-seq signal of 1,245 KDM6A-activated targets from RNA-seq**  
1514 **data at transcription start site (TSS) within 5,000 kb window in sgCTRL and**  
1515 **sgKDM6A#1 in A673 cells.** (F) Scatter plot of H3K27me3 ChIP-seq signal in 3,095,665  
1516 bins of 1 kb in sgCTRL (x-axis) and sgKDM6A#1 (y-axis) ( $R^2=0.326$ , slope=0.631). (G)  
1517 **Boxplot depicting the average ChIP-seq signal of H3K27me3 in 1 kb bins in sgCTRL and**  
1518 **sgKDM6A#1. Bin mapping analysis identified 579,992 and 142,556 bins that gained (up**  
1519 **bins) or loss (down bins) H3K27me3 signal, respectively, upon KDM6A KO compared**  
1520 **to control.** (H) Western blot analysis of KDM6A and BRG1 protein levels in BRG1  
1521 immunoprecipitated protein extracts. Lanes represent two input controls (i), the IgG  
1522 control (IgG), empty lanes (-), and the BRG1 immunoprecipitated samples. (I) Boxplot  
1523 depicting the average ChIP-seq signal of BRG1, EWSR1-FLI1, and KDM6A in sgCTRL  
1524 and sgKDM6A#1 A673 cells. (J) ChIP-qPCR of H3K27me3 enrichment in the enhancer  
1525 region of *CSRPI*, *PCSK2* and *SYT1* and in *SYT1* promoter region upon KDM6A KO  
1526 sgRNA#1 in TC71 cells. *DICER* and *TALI* were used as negative and positive control  
1527 regions, respectively. (K) Same as (J) in the enhancer region of *TSPAN13*, *SYT1* and *IRS2*  
1528 genes upon KDM6A knockdown with shRNA#2 in A673 cells. *DICER* and *TALI* were  
1529 used as negative and positive control regions, respectively. Statistical significance was  
1530 determined by Kruskal-Wallis test with Dunn's multiple comparison correction related to  
1531 sgCTRL (D), Wilcoxon signed-rank test (G and I) and ordinary two way ANOVA test  
1532 with Holm-Šidák multiple comparisons correction (J and K) compared to control. Error  
1533 bars indicate SD (G and I) or SEM (D, J and K) of three independent biological  
1534 experiments. **\*\*\*\* $P < 0.0001$ , \*\* $P < 0.01$ , and \* $P < 0.05$ .**

1535 **Figure S5. KDM6A knockout decreases EwS tumor growth.** (A) Bar chart showing  
1536 cell viability upon KDM6A knockout (sgRNA #1 and 2) in A673 cells compared to non-  
1537 targeting control (sgCTRL) at 3 and 6 days. Values are relative to day 0. (B) Bar charts  
1538 showing number of colonies from Fig. 5A, in parental, sgCTRL and sgKDM6A (sgRNA  
1539 #1 and 2) A673 cells. (C) Spaghetti plots showing tumor volume of xenografts from  
1540 parental, sgCTRL, and sgKDM6A (sgRNA #1 and 2) in A673 cells. (D) Boxplot  
1541 representing tumor volume at 17 days post-injection of parental, sgCTRL, and KDM6A  
1542 KO cells (sgRNA#1) in A673. Each dot represents an individual tumor volume. (E)  
1543 Western blot showing protein levels of KDM6A in 8 representative xenograft tumors

1544 derived from sgCTRL and 4 from sgKDM6A (sgRNA#1 and 2) in A673. Tubulin was  
1545 used as loading control. (F) Immunohistochemistry staining of CD99, KDM6A, Ki67,  
1546 and NF200 on sections of tumors excised from sgCTRL and sgKDM6A (#2) xenografts  
1547 of A673 cells. CD99 was used as positive control for EwS cells, Ki67 for cell  
1548 proliferation, and hematoxylin-eosin for histopathological evaluation of tissue. White  
1549 scale bar represents 50  $\mu\text{m}$ . (G) Boxplot depicting H-score quantification of Ki67 in  
1550 sgCTRL and sgKDM6A (#1 and #2) in immunohistochemistry sections from Fig. 5F and  
1551 S5F. (H) Spaghetti plots showing tumor volume of xenograft tumors from sgCTRL and  
1552 sgKDM6A (sgRNA #1 and 2) (n=9 each) in TC71 cells in nude athymic mice. (I) Kaplan-  
1553 Meier representing the percentage of xenograft tumors that reach a tumor volume of 1000  
1554 mm<sup>3</sup> within days post-injection in sgCTRL and KDM6A KO (sgRNA#1 and 2) in TC71  
1555 cells. (J) Boxplot representing mRNA levels of *NEFH* in a panel of 22 EwS cell lines  
1556 extracted from from Barretina *et al.*(45). Each dot represents individual values for a given  
1557 cell line with A673 cell line colored in red. (K) Violin plot representing mRNA levels of  
1558 *NEFH* in primary tumors from GEO public data repositories including EwS among other  
1559 primary sarcoma tumors including osteosarcoma (OS), rhabdomyosarcoma (RMS), and  
1560 synovial sarcoma (SS). MSCs derived from the healthy bone marrow were included as  
1561 control cells. Statistical significance was determined by ordinary two way ANOVA with  
1562 multiple comparisons correction using Dunnett's test (A) relative to sgCTRL at day 0,  
1563 Kruskal-Wallis test with Dunn's multiple comparison correction (B, D and G) relative to  
1564 sgCTRL, survival analysis was performed by Log-rank (Mantel Cox) test (I) and ordinary  
1565 one-way ANOVA with Holm-Sidak multiple comparison test (K) relative to EwS. Error  
1566 bars indicate SEM; \*\*\*\* $P \leq 0.0001$ , \*\*\* $P \leq 0.001$ , \*\* $P \leq 0.01$ , \* $P < 0.05$ , ns indicates not  
1567 significant.

1568 **Figure S6. Impact of KDM6B knockout in EWSR1-FLI1 targets.** (A) Western blot  
1569 showing levels of H3K27ac, H3K4me1, and H3K27me3 in histone extracts upon  
1570 KDM6B KO with two sgRNA sequences (#1 and #2) in A673 cells. Histone H3 was used  
1571 as loading control. Numbers below represent band quantification of H3K27me3  
1572 normalized to H3 and relative to non-targeting control (sgCTRL). (B) Donut charts (up)  
1573 representing the percentage of significantly upregulated or downregulated targets upon  
1574 KDM6B KO (red indicates downregulated targets: 354 and 377 genes for sgKDM6B#1  
1575 and #2, respectively) in A673 cells. Bar chart (below) representing the top five enriched  
1576 gene ontology (GO) biological processes and their associated P-value of the set of  
1577 differentially expressed genes for KDM6B KO. (C) Western blot showing levels of  
1578 KDM6A, and KDM6B in whole cell extracts upon KDM6B KO with two sgRNA  
1579 sequences (#1 and #2) in TC71 cells. Tubulin was used as loading control. (D) RT-qPCR  
1580 of KDM6B-EWSR1-FLI1 targets in sgKDM6B#1 and #2 TC71 cells. *GAPDH* was used  
1581 as housekeeping gene. (E) Metagene plot showing H3K27me3 ChIP-seq signal of 266  
1582 KDM6B-activated targets from RNA-seq data at transcription start site (TSS) within  
1583 5,000 kb window in sgCTRL and sgKDM6B#2 in A673 cells. (F) Scatter plot of  
1584 H3K27me3 ChIP-seq signal in 3,095,665 bins of 1 kb in sgCTRL (x-axis) and  
1585 sgKDM6B#1 (y-axis) ( $R^2=0.285$ , slope=0.501). (G) Boxplot depicting the average ChIP-  
1586 seq signal of H3K27me3 in 1 kb bins in sgCTRL and sgKDM6B#2. Bin mapping analysis  
1587 identified 380,371 and 442,200 bins that gained (up bins) or loss (down bins) H3K27me3  
1588 signal, respectively, upon KDM6B KO compared to control. (H) Western blot (above)  
1589 showing levels of H3K27me3 in histone extracts of TC71 cells treated with vehicle or the  
1590 demethylase inhibitor GSKJ4 at 2.5 and 5  $\mu\text{M}$  (+ and ++, respectively) for 72h. Histone  
1591 H4 was used as loading control. Numbers below represent band quantification of  
1592 H3K27me3 normalized to H4 and relative to vehicle control. RT-qPCR (below)

1593 determination of EWSR1-FLI1 targets with both KDM6A and KDM6B or with KDM6B  
1594 ChIP-seq peaks (A-B-EF and B-EF groups, respectively) in TC71 cells treated with  
1595 vehicle or GSK-J4 at 2.5  $\mu$ M for 72 hours. *TBP* was used as housekeeping gene. (I) Table  
1596 showing top MEME DNA motifs and the corresponding E-value for BRG1 ChIP-seq  
1597 peaks in A673 cells. (J) **Western blot analysis of KDM6B and BRG1 protein levels in**  
1598 **BRG1 immunoprecipitated protein extracts. Lanes represent two input controls (i), the**  
1599 **IgG control (IgG), empty lane (-), and the BRG1 immunoprecipitate samples. (I)**  
1600 Statistical significance was determined by Kruskal-Wallis test with Dunn's correction for  
1601 multiple comparison (D), Wilcoxon signed-rank test (G) and Student t-test (H) related to  
1602 control group. Error bars in (D and H) indicate SEM of three independent biological  
1603 experiments; \*\*\*\* $P < 0.0001$ , \*\* $P < 0.01$  and \* $P < 0.05$ .

1604 **Figure S7. KDM6B knockout decreases tumor growth and sensitizes EwS cells to**  
1605 **the EZH2 inhibitor GSK126.** (A) Bar charts representing colony number, from colony  
1606 assay in Figure 7A of parental, sgCTRL and sgKDM6B (sgRNA #1 and 2) A673 cells.  
1607 (B) Colony formation assay of KDM6B KO cells (sgRNA#1 and 2) compared to sgCTRL  
1608 in TC71 cells. (C) Bar charts representing colony number, from colonies in Figure S7B  
1609 in sgCTRL and sgKDM6B (sgRNA #1 and 2) TC71 cells. (D) Annexin V staining of  
1610 sgCTRL and sgKDM6B#2 A673 cells treated with vehicle or GSK126 inhibitor at 15  $\mu$ M  
1611 for 24 hours. Numbers indicate percentage of cells in each quadrant. (E) Same as in (D)  
1612 with sgKDM6A#1 in A673. (F) Western blot showing levels of KDM6A, cleaved-PARP-  
1613 1 (c-PARP), and phosphorylation of S139 in variant gamma-H2A.x ( $\gamma$ -H2Ax) in whole  
1614 cell extracts (above) and H3K27me3 in histone extracts (below) from sgCTRL and  
1615 sgKDM6A#1 A673 cells treated with vehicle or GSK126 inhibitor (15  $\mu$ M for 24 hours).  
1616 Tubulin and histone H3 were used as loading controls for whole cell or histone extracts,  
1617 respectively. Numbers below represent band quantification of H3K27me3 normalized to  
1618 H3 and relative to sgCTRL or sgKDM6A#1 treated with vehicle. (G) **Bar plot showing**  
1619 **percent of viable, early and late apoptotic and necrotic cells by Annexin V staining, in**  
1620 **sgCTRL, sgKDM6B#2 and cells overexpressing a wild-type (wt) or catalytic-dead (mut)**  
1621 **form of KDM6B in A673 cells treated with vehicle or GSK126 (15  $\mu$ M for 24h).** (H)  
1622 Heatmap and dendrogram showing expression of genes within the Hallmark collection of  
1623 Double Strand Break Repair from GSEA analysis in shCTRL and shKDM6B#2, that are  
1624 significantly upregulated upon KDM6B knockdown in A673 cells. n, indicates number  
1625 of deregulated targets upon KDM6B knockdown. Statistical significance was determined  
1626 by Kruskal-Wallis test with Dunn's correction for multiple comparison (A and C) relative  
1627 to sgCTRL **and ordinary two-way ANOVA test with Dunnett's multiple comparison**  
1628 **correction relative sgCTRL treated with vehicle (G).** Error bars indicate SEM of three  
1629 independent biological experiments. \*\*\*\*  $P \leq 0.0001$ , \*\*\* $P < 0.001$ , \*\* $P \leq 0.01$ , \* $P \leq 0.05$   
1630 and ns indicates not significant.

1631 **Other Supplementary Materials for this manuscript include the following:**

1632 **Supplementary Table S1.** Excel file showing genes associated to gain or loss of bins of  
1633 H3K27me3 (up or down bins, respectively) following EWSR1-FLI1 introduction in  
1634 hpMSC.

1635 **Supplementary Table S2.** Excel file with summary of KDM6A, KDM6B and FLI1  
1636 Diffbind peaks from ChIP-seq data in A673 cells.

- 1637 **Supplementary Table S3.** Excel file with the associated list of genes for KDM6A and  
1638 KDM6B ChIP-seq peaks in A673 cells.
- 1639 **Supplementary Table S4.** Excel file showing differential expressed genes of shKDM6A  
1640 and shKDM6B with shRNA sequences #1 and #2 in A673 cells, **the list of EWSR1-FLI1-**  
1641 **KDM6A or EWSR1-FLI1-KDM6B targets downregulated upon KDM6A or KDM6B**  
1642 **knockdown in A673 cells** and the core enriched EMT gene sets upon knockdown of  
1643 KDM6A or KDM6B.
- 1644 **Supplementary Table S5.** Excel file **showing differential expressed genes of sgKDM6A**  
1645 **and sgKDM6B with sgRNA sequences #1 and #2 in A673 cells, and the list of EWSR1-**  
1646 **FLI1-KDM6A or EWSR1-FLI1-KDM6B targets downregulated upon KDM6A or**  
1647 **KDM6B KO in A673 cells.**
- 1648 **Supplementary Table S6.** Excel file with the list of genes from the Double Strand Break  
1649 Repair category from GSEA analysis significantly upregulated upon KDM6B  
1650 knockdown in A673 cells.
- 1651 **Supplementary Table S7.** Excel file with information of the antibodies, primers, and  
1652 RNAi and CRISPR sequences used.

# Figure 1

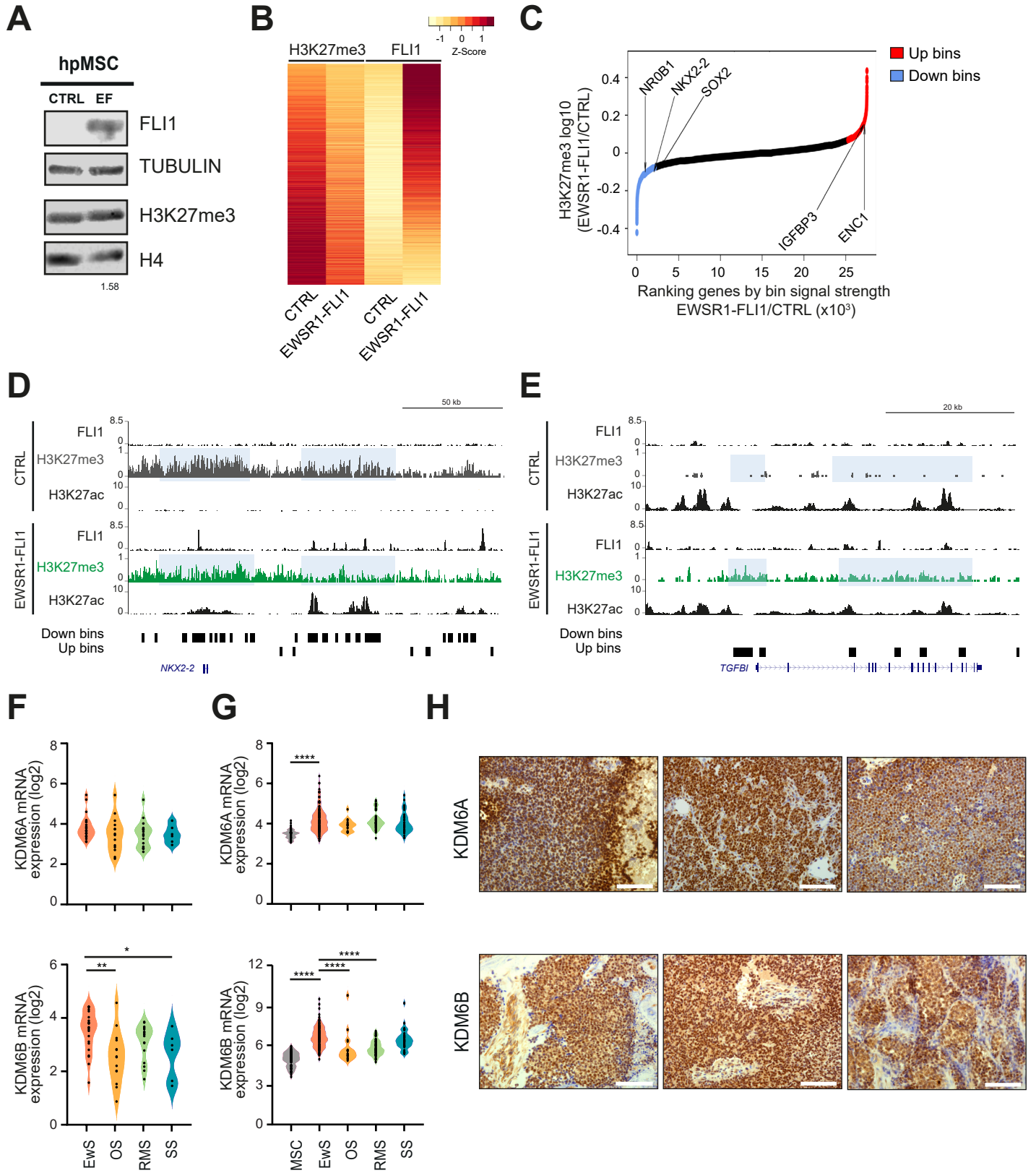


# Figure 2

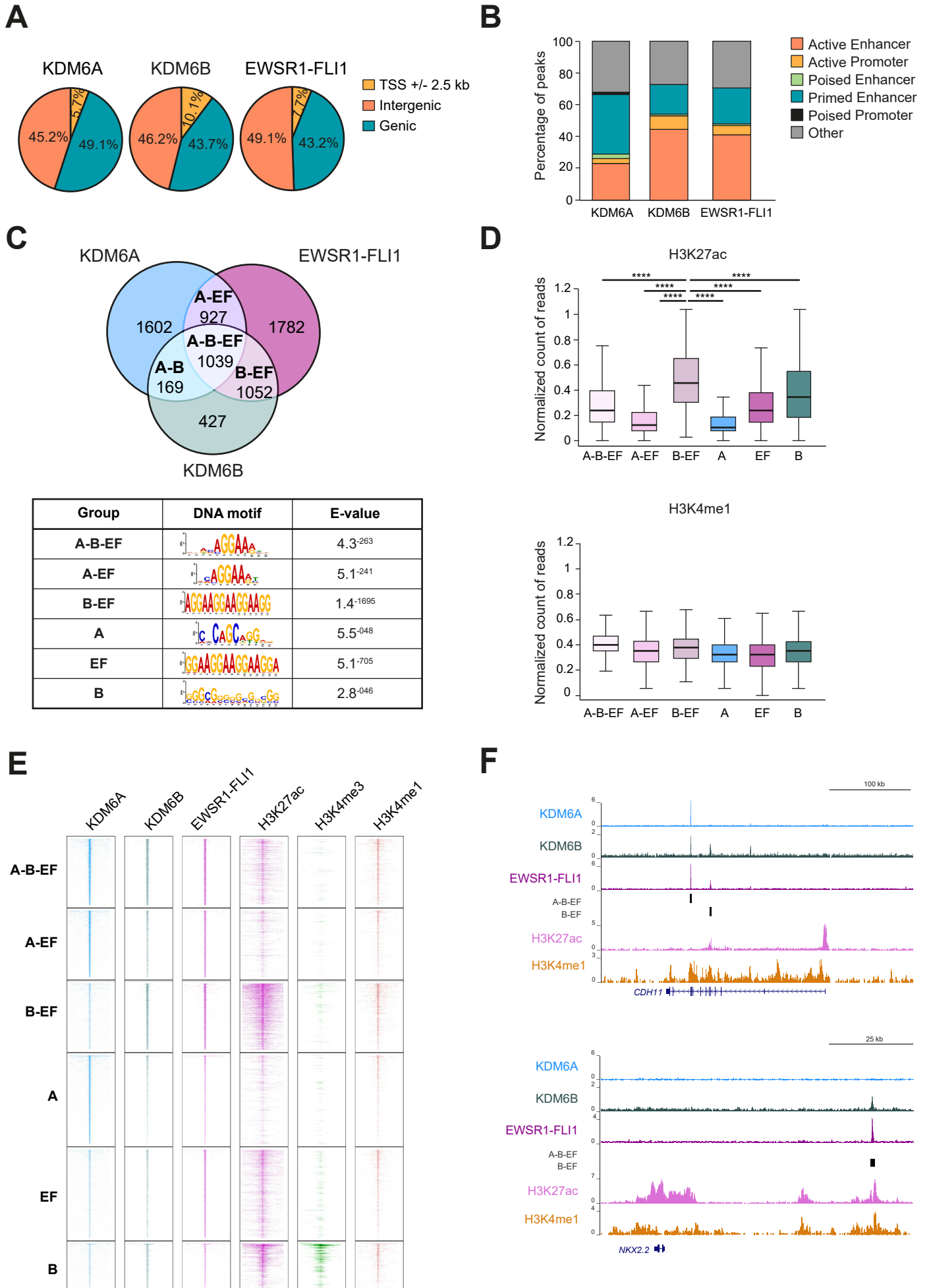


# Figure 3

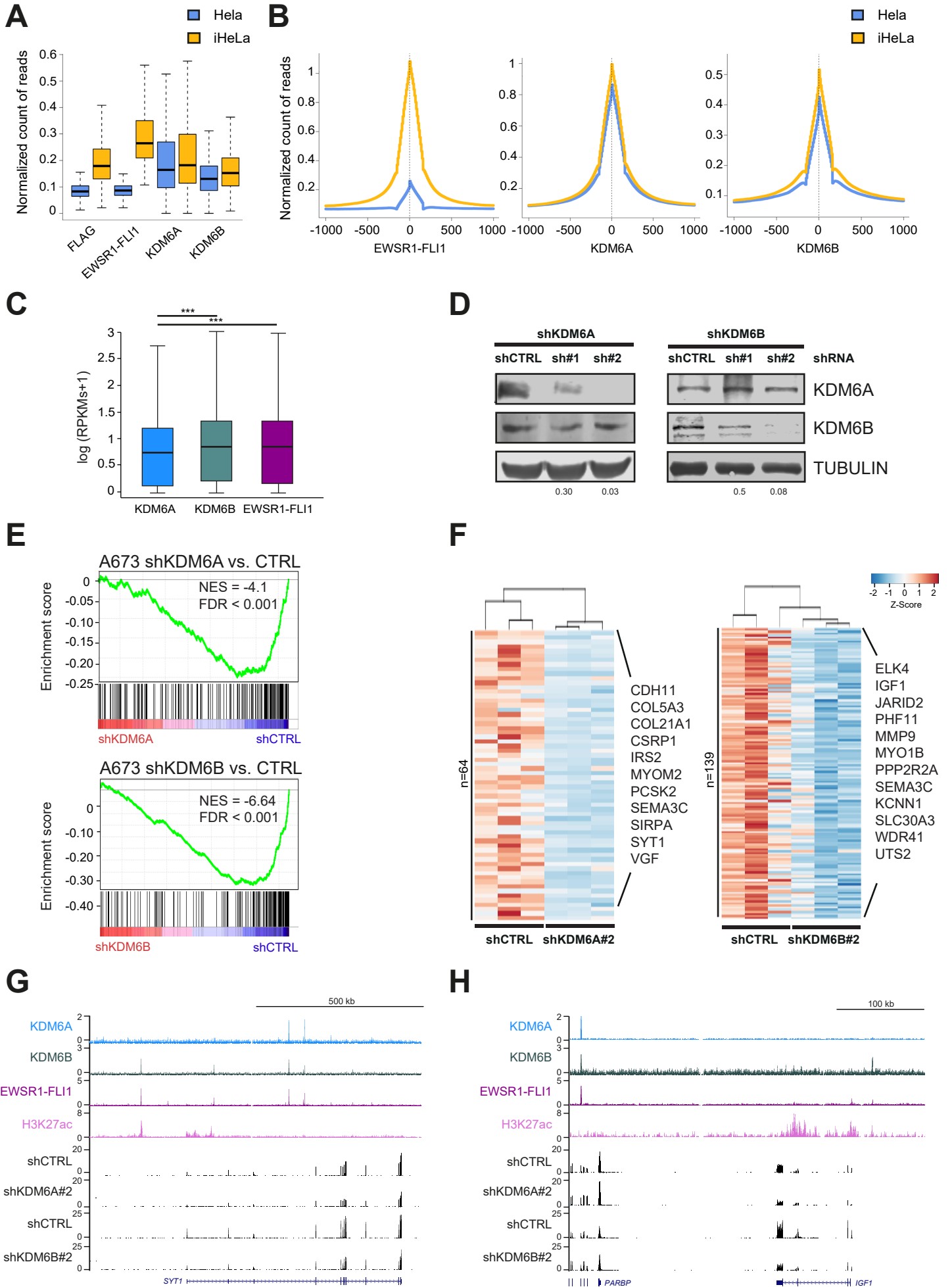




**Figure 4**

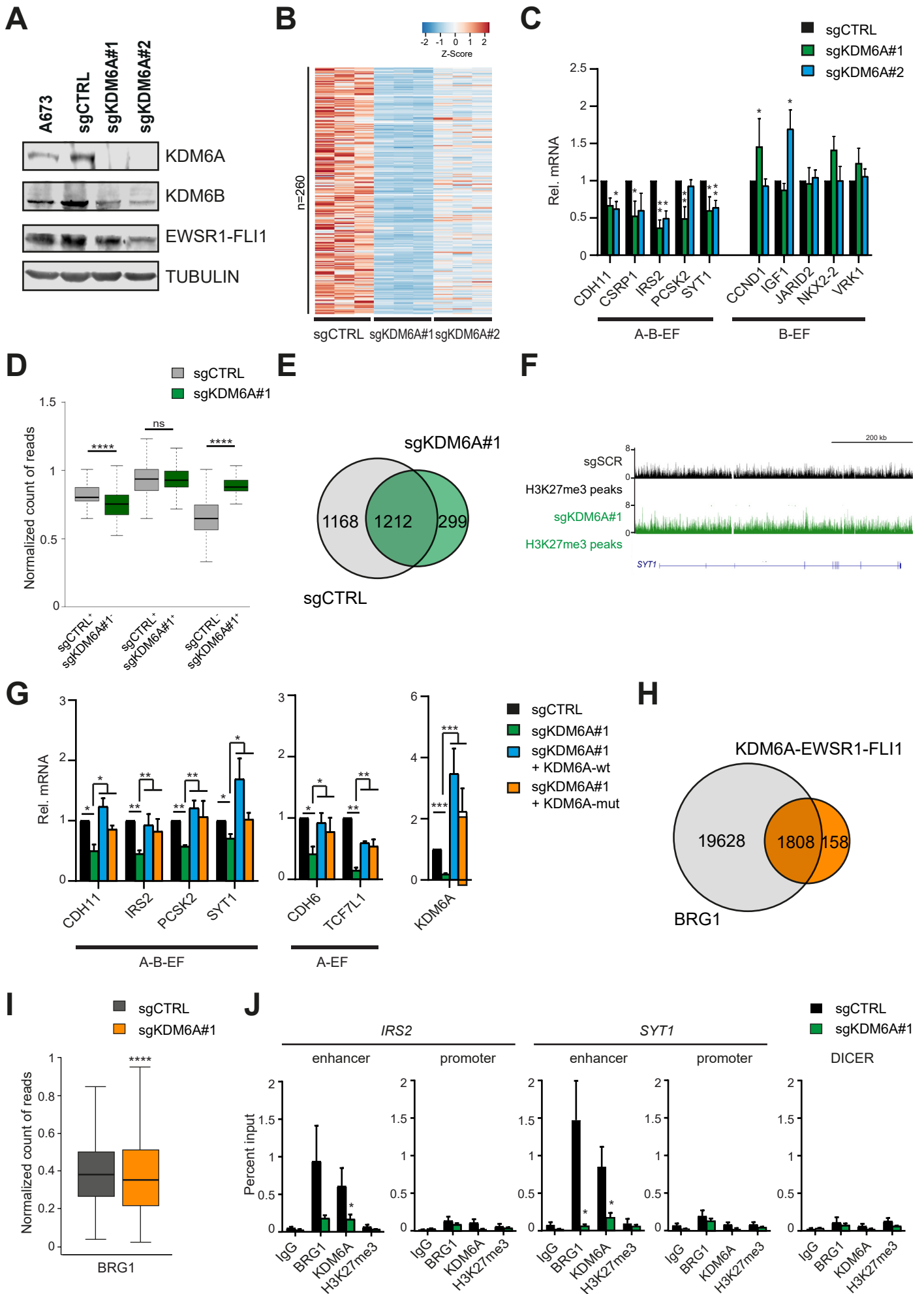


**Figure 5**

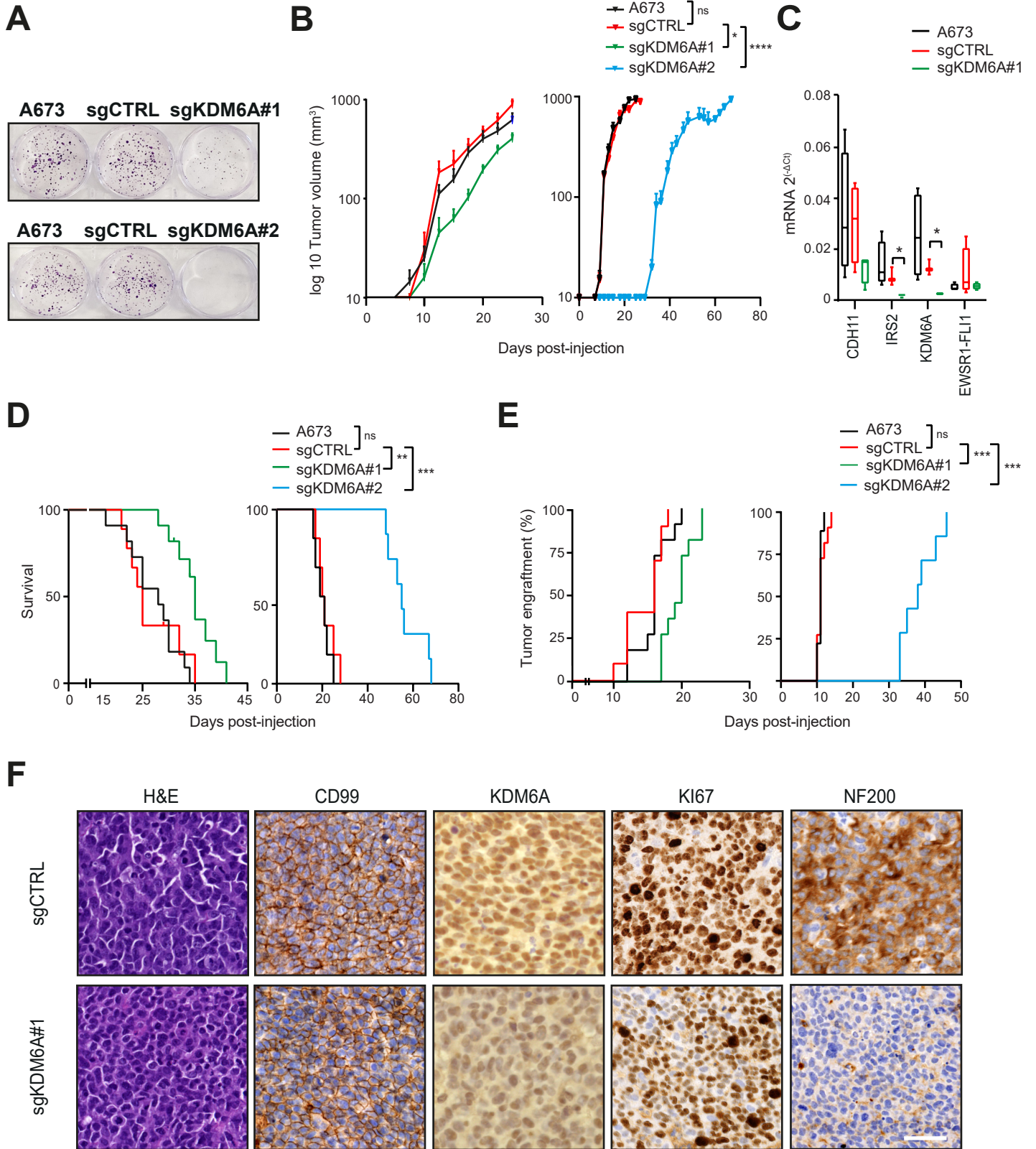


**Figure 6**

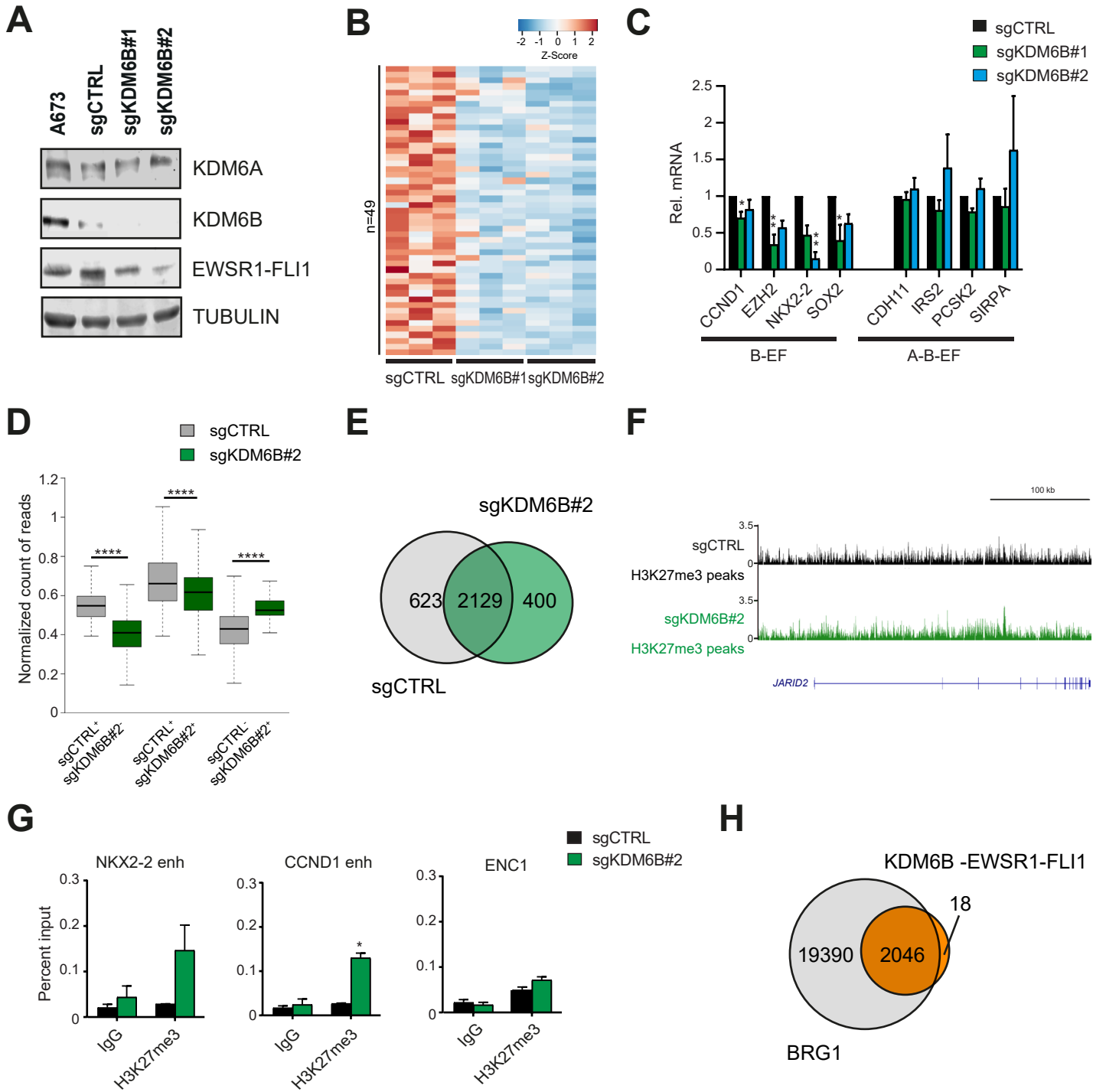
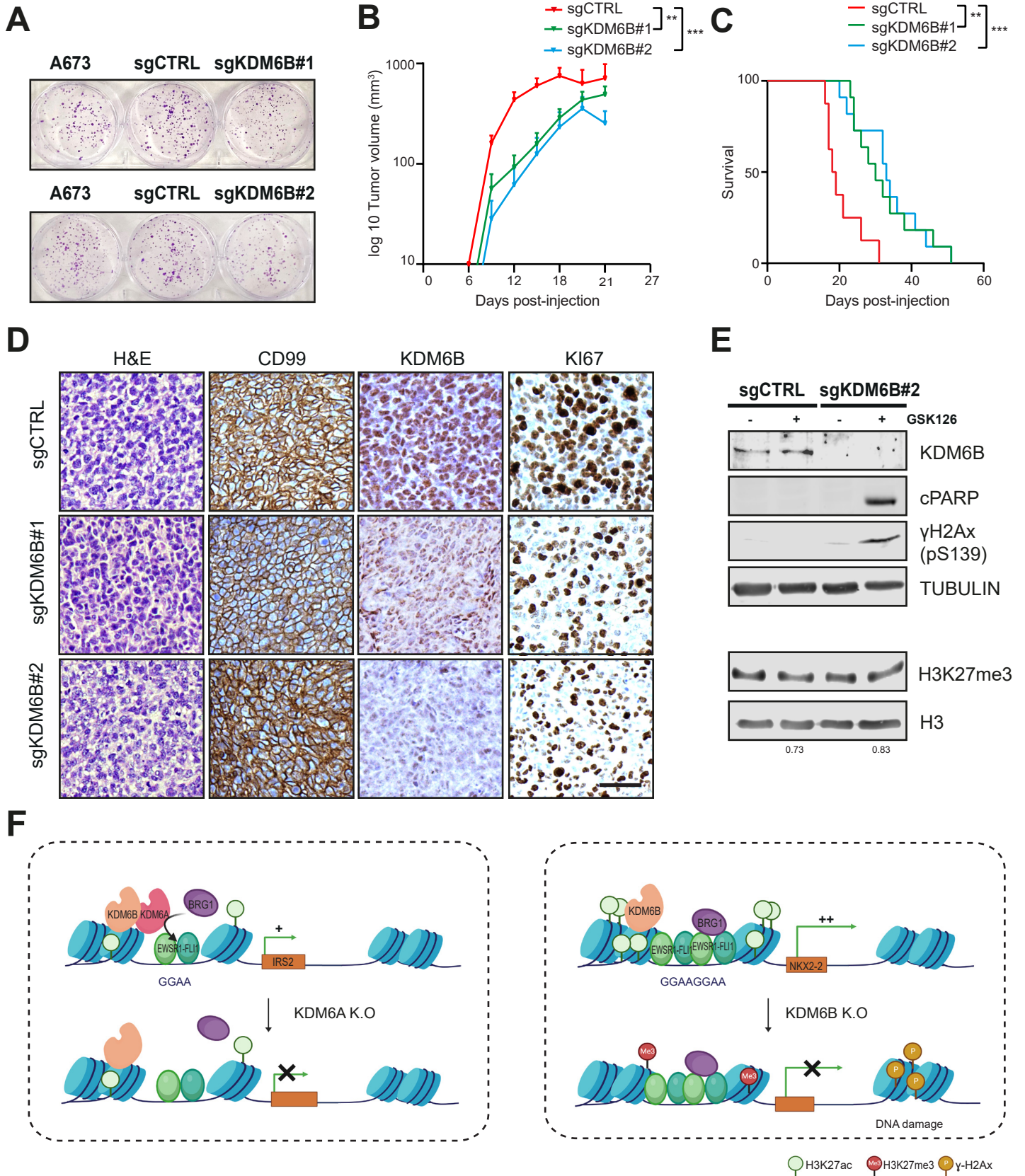
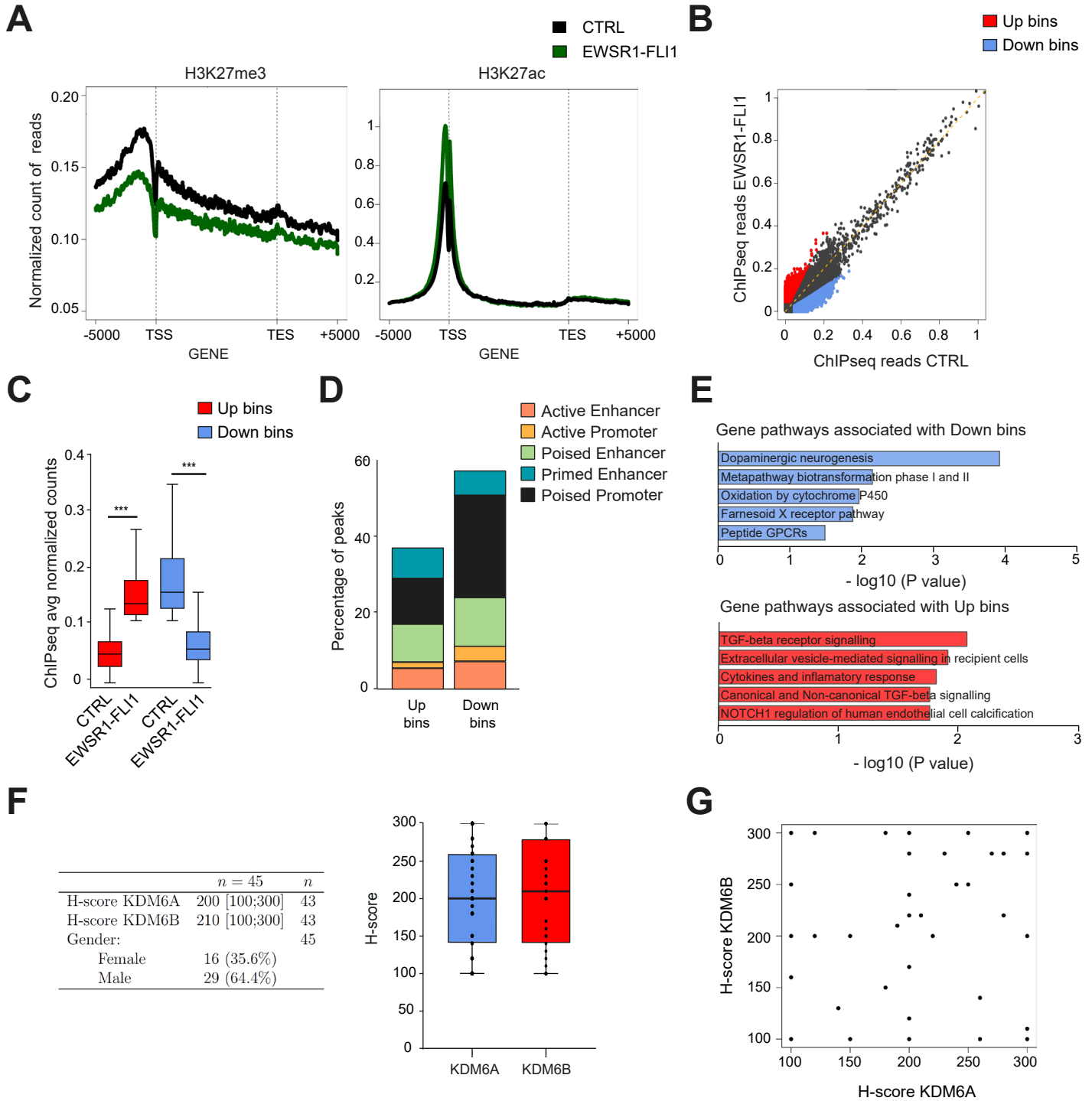


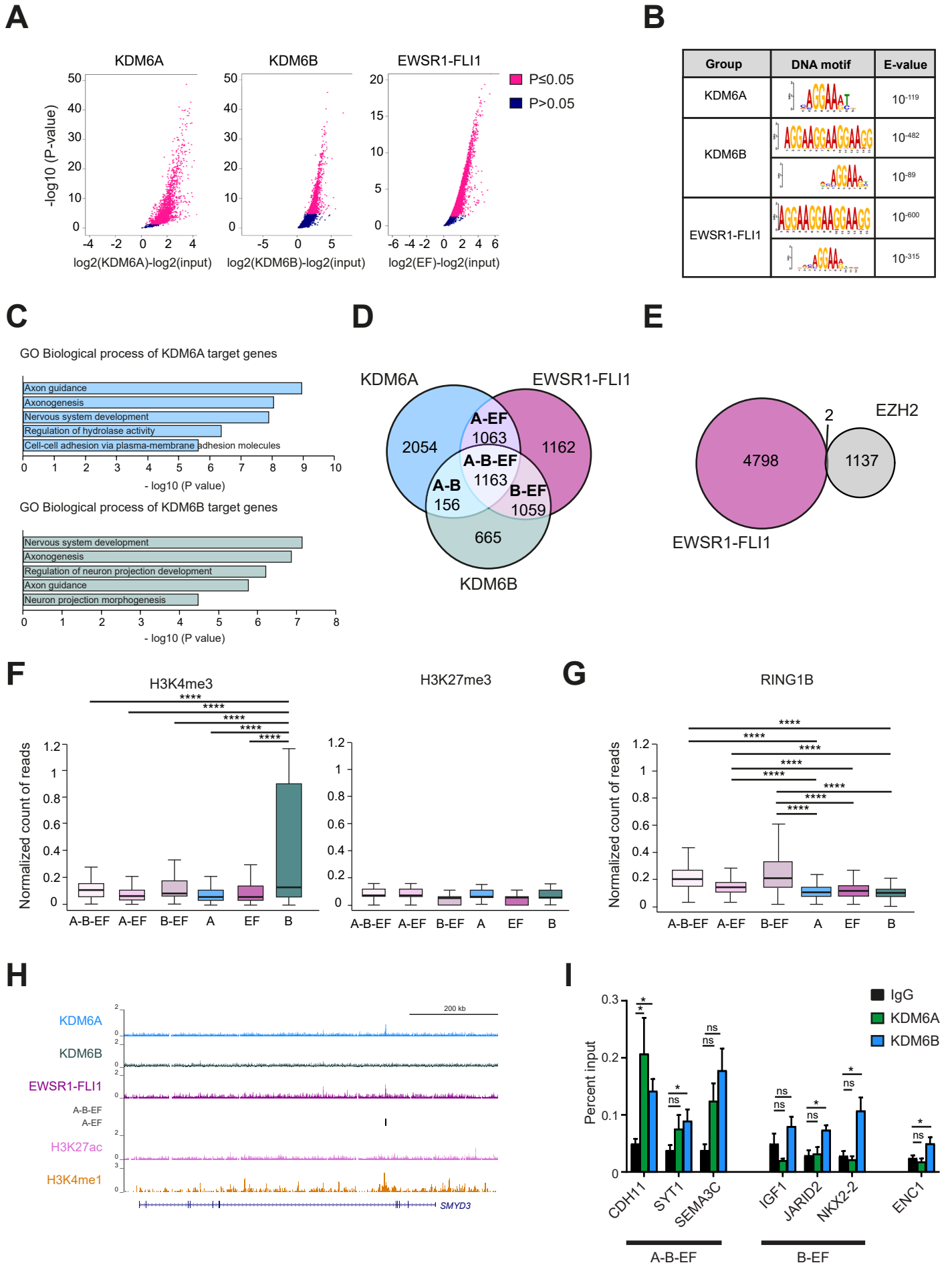
# Figure 7



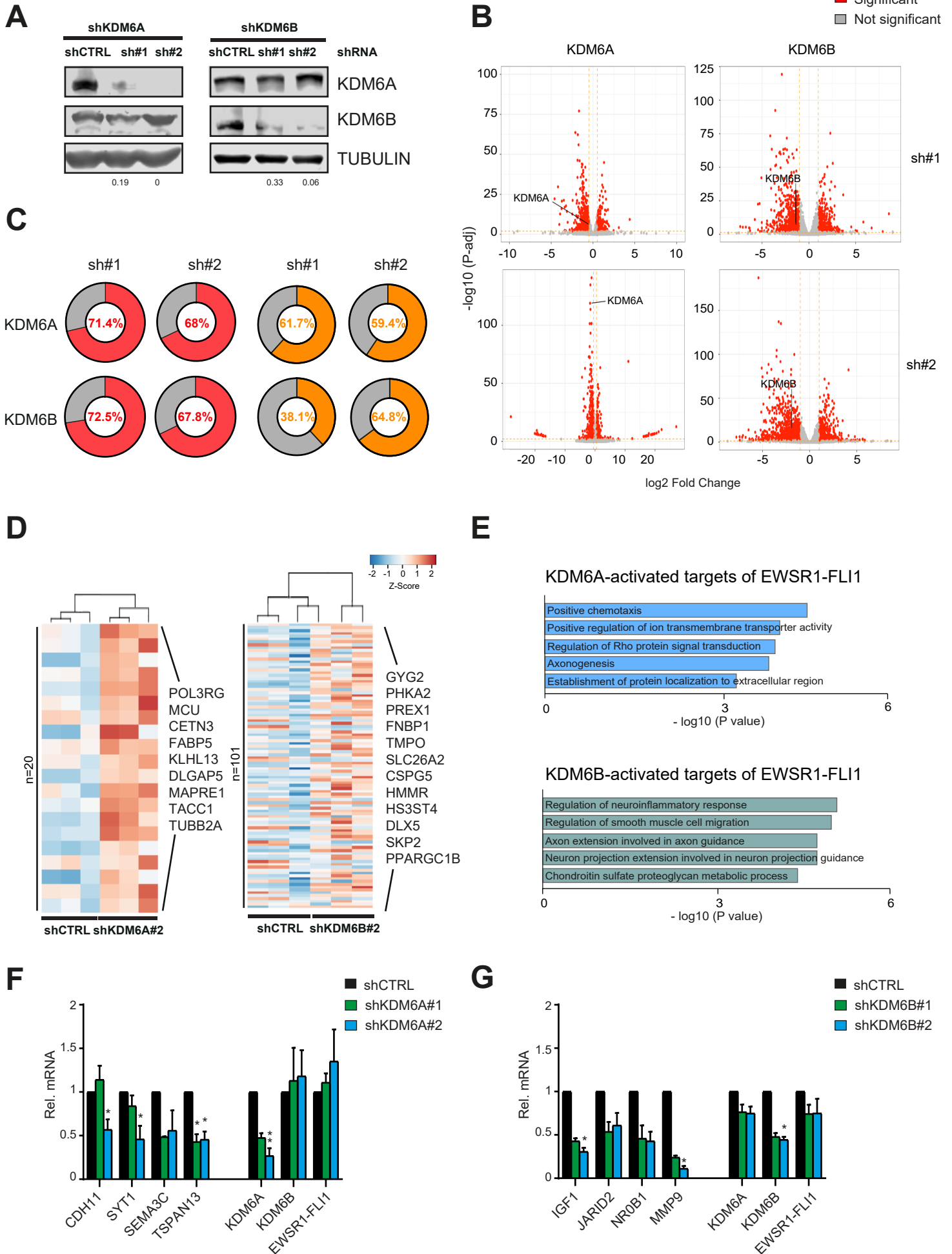
# Supplementary Figure 1



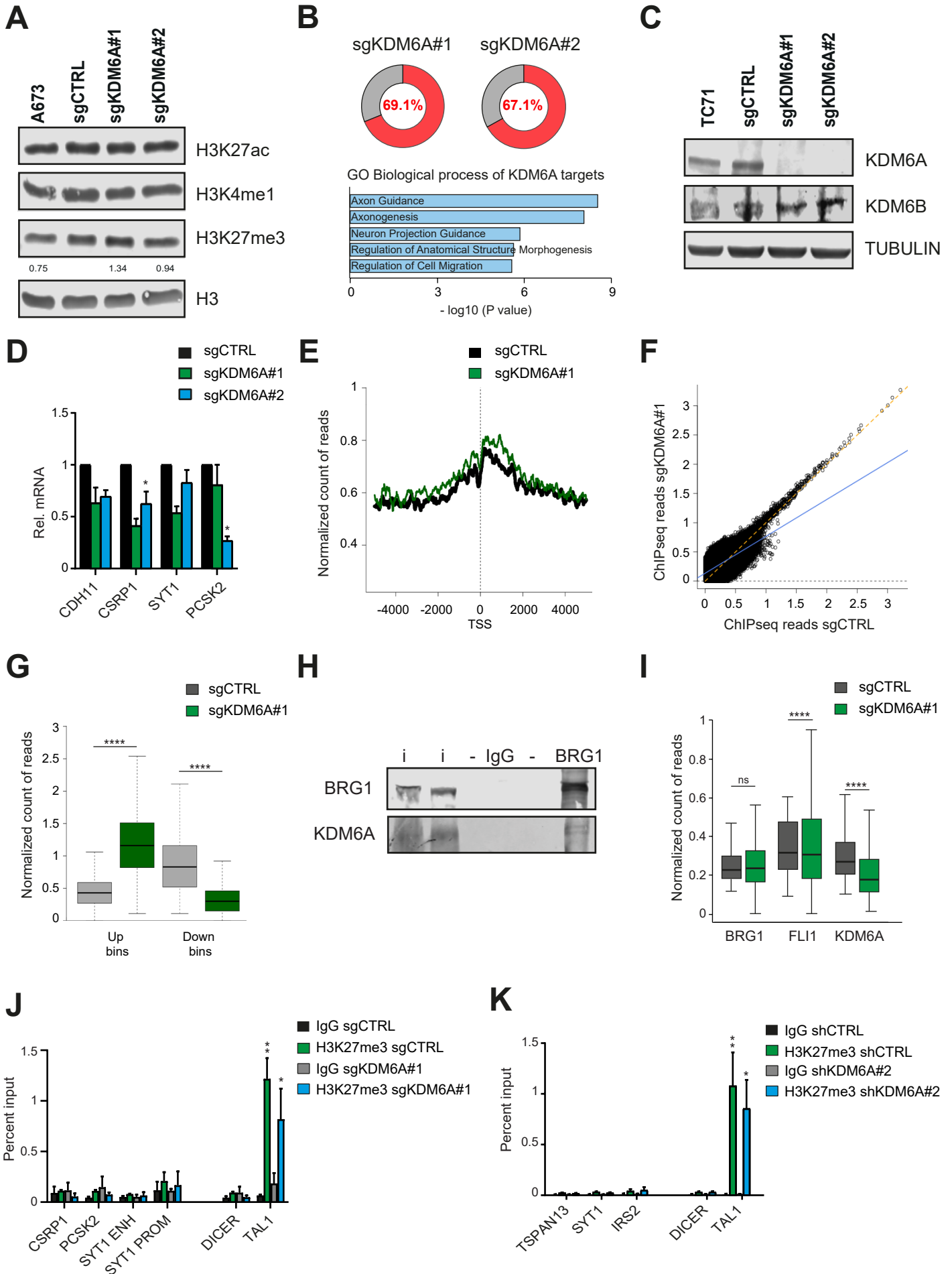
# Supplementary Figure 2



# Supplementary Figure 3

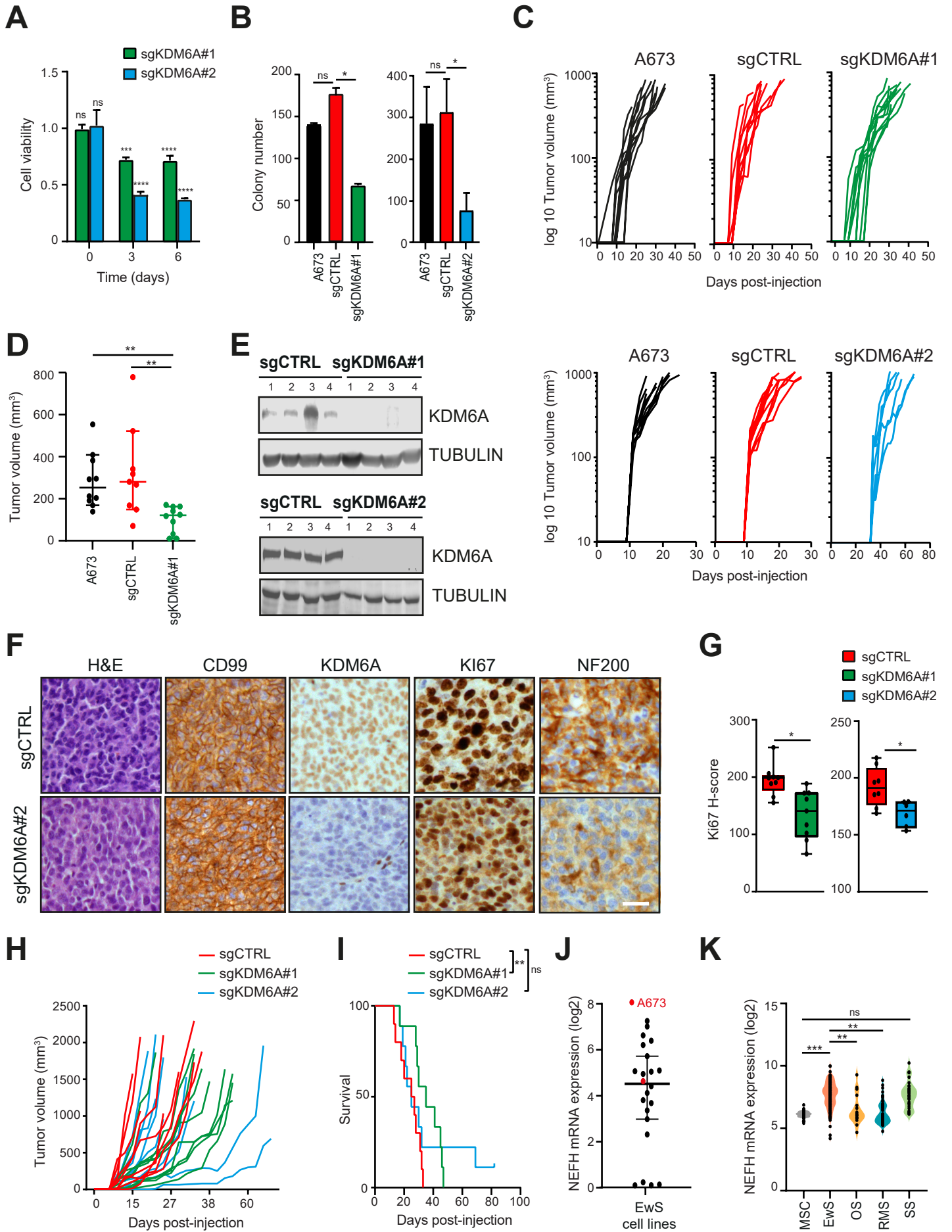


# Supplementary Figure 4





# Supplementary Figure 5





# Supplementary Figure 7

